Algorithm Identification: Case II.S Bright Pixel Atmospheric Correction

Table of Contents

1. Introduction 6

2. Evolution and Status 6

3. Algorithm Overview 7

4. Algorithm Description 7

4.1 Theoretical Description 7

4.1.1 Hydrological Model 7

4.1.2 Implementation of the Hydrological Model 10

4.1.3 Atmospheric model 12

4.2 Hydrological Model Parameters 14

4.2.1 Pure Water Absorption 14

4.2.2 Pure Water Scattering 15

4.2.3 Particulate Absorption 16

4.2.4 Particulate Scattering 16

4.2.5 Chlorophyll Absorbance and Fluorescence 17

4.3 Model Sensitivity 20

4.3.1 Similarity and Optimal Band Choice 20

4.3.2 Temperature and Smile 22

4.3.3 MERIS radiometric sensitivity and Aerosol retrieval error 23

4.4 Implementation 25

4.4.1 Rayleigh correction 25

4.4.2 Temperature and Smile Offsets 25

4.4.3 Choice of IOPs 26

4.4.4 Initial Estimates 27
4.4.5 Band Choice 28
4.4.6 Radiometric Thresholding 29
4.4.7 Determination of bb from $\rho_w(\lambda)$ 30
4.4.8 Low Band Solution 30
4.4.9 High Band Solution 31
4.4.10 Estimate combination 32
4.4.11 TSM Estimates 33
4.4.12 ODESA output 33
4.4.13 Derived flags 33
5. Parameter Description 33
5.1.1 Error Budget Estimates 34
5.1.2 Practical Considerations 34
5.1.3 Sensitivity to IOPs 35
5.2 Practical Considerations 35
5.2.1 Calibration and Validation 35
5.2.2 Quality Control and Diagnostics. 37
5.2.3 Exception Handling 37
5.2.4 Output Product 37
6. Assumptions and Limitations 37
7. References 37

Figures

Figure 1: The (a) relationship between suspended sediment and reflectance and (b) relationship between the reciprocals of suspended sediment and reflectance. Data taken from Lavender (2006). 9
Figure 2: F' vs. eta and bb/(a+bb) 11
Figure 3: Variation in Water absorption from literature 14

Figure 4: Temperature dependence of water absorption 15

Figure 5: Reflectance saturation - Severn Estuary 16

Figure 6: Chlorophyll fluorescence and absorption for MERIS Bands.....17

Figure 7: Effects of natural fluorescence on BPAC 18

Figure 8: Similarity spectrum for low band set 21

Figure 9: Similarity spectrum for high band set.....22

Figure 10: Sensitivity to Temperature - low band set.....22

Figure 11: Sensitivity to 1 nm smile low band set.....23

Figure 12: MERIS Counts vs. sediment load 24

Figure 13: Aerosol retrieval errors vs. MERIS Counts 25

Figure 14: White scatter Flag 26

Figure 15: Comparative scattering in Severn Estuary and Barents Sea 27

Figure 16: BPAC Initial Estimates.....29

Figure 15: $\rho_w(705)$ images from v5.0 and v4.1.....35

Figure 16: $\rho_w(775)$ and α retrievals for Severn transect.....36

Figure 17: $\rho w(412)$ and $\rho w(490)$ retrievals for Severn transect 36

Tables

Table 1: Fluorescence height and phytoplankton absorption 20

Nomenclature

Δ_ϕ	Sun-sensor viewing azimuth difference	degrees
λ	Wavelength	nm
θ_v	Sensor viewing zenith angle (the satellite "look angle")	degrees
θ_s	Solar zenith angle	degrees
ρ	Fresnel reflectance at normal incidence	dimensionless
ρ_a	Multiple scattering aerosol reflectance	dimensionless
ρ_{as}	Single scattering aerosol reflectance	dimensionless
ρ_g	Reflectance due to sun glitter	dimensionless
ρ_r	Rayleigh reflectance	dimensionless
ρ_{ra}	Reflectance due to Rayleigh-aerosol interaction	dimensionless
ρ_t	Top of atmosphere reflectance	dimensionless
ρ_w	Water reflectance (above surface)	dimensionless
$\tilde{\rho}$	Fresnel reflectance for sun and sky irradiance	dimensionless
τ_{oz}	Ozone optical thickness	m^{-1}
τ_{wv}	Water vapour optical thickness	m^{-1}
τ_r	Rayleigh optical thickness	m^{-1}
a	Total absorption coefficient	m^{-1}
a^*_{bb}	Sediment absorption to backscatter ratio	dimensionless
a_p	Combined (phytoplankton, detritus, sediment and gelbstoff) absorption coefficient	m^{-1}
a_s	Particulate specific absorption	m^{-1}
a_w	Water absorption coefficient	m^{-1}
b	Total scattering coefficient	m^{-1}
bb	Total backscattering coefficient	m^{-1}
bb_p	Particulate (phytoplankton, detritus and sediment) backscattering coefficient	m^{-1}
bb_w	Water scattering coefficient	m^{-1}
$\tilde{b}$	Particulate backscattering ratio	dimensionless
c	Variable given in Gordon and Wang (1994)	dimensionless

f	Empirical factor relating IOPs to R	dimensionless
f'	Empirical factor relating IOPs to R	dimensionless
F	Empirical factor relating IOPs to ρ_w	dimensionless
F'	Empirical factor relating IOPs to ρ_w	dimensionless
n_w	Refractive index of seawater	dimensionless
r	Air-water reflectance for diffuse irradiance	dimensionless
t	Diffuse atmospheric transmittance	dimensionless
Q	Ratio of upwelling irradiance to radiance	dimensionless
R	Irradiance reflectance	dimensionless

1. Introduction

The successful exploitation of remotely sensed water colour observations requires the development of atmospheric correction methods in coastal waters, and the determination of total suspended matter (TSM) concentrations in gravimetric units for use in mass flux studies and hydrodynamic models. By definition, Case 1 waters (stratified shelf seas and the deep ocean) are coloured by biogenic materials alone (phytoplankton, its pigments, dissolved organic exudates and detritus). Coastal waters are usually termed Case II because the major influence on the water colour is TSM (primarily tidally stirred sediments or riverine fluvial muds) or gelbstoff (yellow substances). Gelbstoff is mainly dissolved coloured organic material (CDOM), consisting of humic and fluvic compounds of terrestrial origin that are transported into marine waters by river/estuary systems.

With even modest concentrations of TSM (>0.2 g m^{-3}), there is significant backscatter that results in reflectance at near infra-red wavelengths (NIR) that negates the `dark pixel' atmospheric correction (AC) procedures, which assume zero water leaving at NIR wavelengths (> 700 nm). These are termed `bright pixel' waters and require a modified bright pixel atmospheric correction (BPAC). In addition, when phytoplankton such as coccolithophores are abundant the water can also be highly reflective (at visible and NIR wavelengths) due to backscatter from detached coccoliths and the BPAC is also invoked. Very high concentrations of any phytoplankton particles will also give significant backscatter and again the BPAC will be required to correct for the resultant NIR reflectance.

Gelbstoff has little effect on the atmospheric correction (`dark pixel'), as it primarily absorbs due to its dissolved nature, but Case 2 algorithms are needed for the retrieval of the concentrations of gelbstoff and other optically active components of the water such as TSM and chlorophyll-a (Chl-a).

2. Evolution and Status

It's foreseen that the ATDB will evolve in the short-term. In particular there are specific issues to address:

- Basic sensitivity tests have only been carried out using the low band set – since fitting methods may evolve in the short term.
- The band sets and fitting methods may evolve – in particular alpha may be constrained using the 412 band.
- White scatterers are not currently parameterised.
- The current atmospheric model does not account for the surface albedo.

3. Algorithm Overview

In waters dominated by sediment there is significant water leaving radiance at both visible and NIR wavelengths. An AC based on the concept of zero NIR water leaving radiance (dark pixel model) will fail because the extrapolation of aerosol path reflectance into visible bands will result in apparent negative reflectance at visible wavelengths; overcorrection due to an overestimation of the aerosol scattering.

The conventional AC procedures that were applied to CZCS and SeaWiFS (e.g. Antoine and Morel, 1991 and Gordon and Wang, 1994) assumed a dark pixel; zero NIR water reflectance. To undertake the bright pixel component SeaWiFS initially used an iterative method (Siegel *et al*. 2000) to correct for non-negligible water reflectance in the NIR arising from moderate to high phytoplankton abundances (chlorophyll concentrations greater than ~2 mg m^{-3}) and so independent research was applied to correct for the effects of TSM (e.g. Ruddick *et al.* 2000 and Lavender *et al.* 2005), but the processing software has now been updated so that it takes non-phytoplankton scattering (Arnone *et al.* 1998) into account for both MODIS and SeaWiFS (Stumpf *et al.* 2002). In addition, research has investigated longer wavelengths where the water signal can still be assumed to be negligible (Wang and Shi, 2005).

The MERIS BPAC assumes there is significant water reflectance, as detected by the Case II.S Turbid Water flag ATBD 2.5, and partitions the top of the atmosphere reflectance, ρ_t, into components due to aerosols and in-water particles (TSM) using a coupled hydrological and atmospheric model. The hydrological model assumes that the surface water reflectance, $\rho_w(\theta_s,\theta_v,\Delta_\phi)$, can be determined by the absorption of water together with the absorption and scattering of particles. Reflectance has an angular dependence described by the solar zenith angle (θ_s), viewing zenith angle (θ_v) and difference (solar versus viewing) in the azimuth angles (Δ_ϕ).

The atmosphere is modelled using a simple single scattering model, which assumes that the atmospheric path radiance and absorption can be separated into the Rayleigh and aerosol components. The aerosol component is modelled by a simple angstrom exponent.

4. Algorithm Description

4.1 Theoretical Description

4.1.1 Hydrological Model

The hydrological optics depends on the inherent optical properties (IOPs) of the TSM, which varies according to wavelength (λ). Parameterisation of reflectance for waters dominated by TSM involves knowledge of three IOPs and their spectral properties: particulate specific absorption, $a_s(TSM,\lambda)$; particulate specific scattering, $b_s(TSM,\lambda)$; particulate backscattering ratio, $\tilde{b}$. The sensitivity of these IOPs with regard to sediment type has been investigated, under laboratory conditions, using measurements of reflectance with a spectroradiometer

above a 2m depth tank (Bale *et al*., 1994). The tank depth simulated optically deep water, as pure water at NIR wavelengths has a high attenuation coefficient; 1.53 m^{-1} at 700 nm and 0.20 m^{-1} at 865 nm.

Figure 1a shows the relationship between reflectance and TSM (termed Suspended Particulate Matter, SPM, in Lavender 2006) for sediments collected around the UK (primarily the east and south coasts). The reflectance shows high variation between sediment types, but each curve shows a non-linear relationship between sediment concentration and reflectance. Figure 1b shows the relationship between the reciprocal of sediment concentration and the reciprocal of remote sensed reflectance. It can be observed that this is a quasi-linear within relationship. This relationship can be explored further by considering the theoretical relationship with reflectance, $\rho_w(\theta_s,\theta_v,\Delta_\phi)$, expressed as:

$$\rho_w = \pi\Re\frac{f(\theta_s,\theta_v,\Delta\phi)}{Q(\theta_s,\theta_v,\Delta\phi)}\left(\frac{bb_w + bb_{pds}}{a_w + a_{pdsg}}\right) \quad (1a)$$

or alternatively:

$$\rho_w = \pi\Re\frac{f'(\theta_s,\theta_v,\Delta\phi)}{Q(\theta_s,\theta_v,\Delta\phi)}\left(\frac{bb_w + bb_p}{a_w + a_p + bb_w + bb_p}\right) \quad (1b)$$

Where $\Re$ is defined as:

$$\Re = \left[\frac{(1-\rho)(1-\tilde{\rho})}{n_w^{\,2}}\right] \quad (2)$$

n_w is the refractive index of seawater, ρ is the Fresnel reflectance at normal incidence, $\tilde{\rho}$ is the Fresnel reflectance for sun and sky irradiance, r is the air-water reflectance for diffuse irradiance; these reflectances are dependent on the sea state for which wind speed is taken as a proxy.

Q is the ratio of upwelling irradiance to radiance, while f and f' are quasi constants for case 1 waters; all of these are dependent on the viewing geometry.

a_w, bb_w are the absorption and backscatter of water, bb_p is the combined backscatter of phytoplankton, detritus and sediment; a_p is the combined absorption of phytoplankton, detritus, sediment and gelbstoff (CDOM).

a)

b)

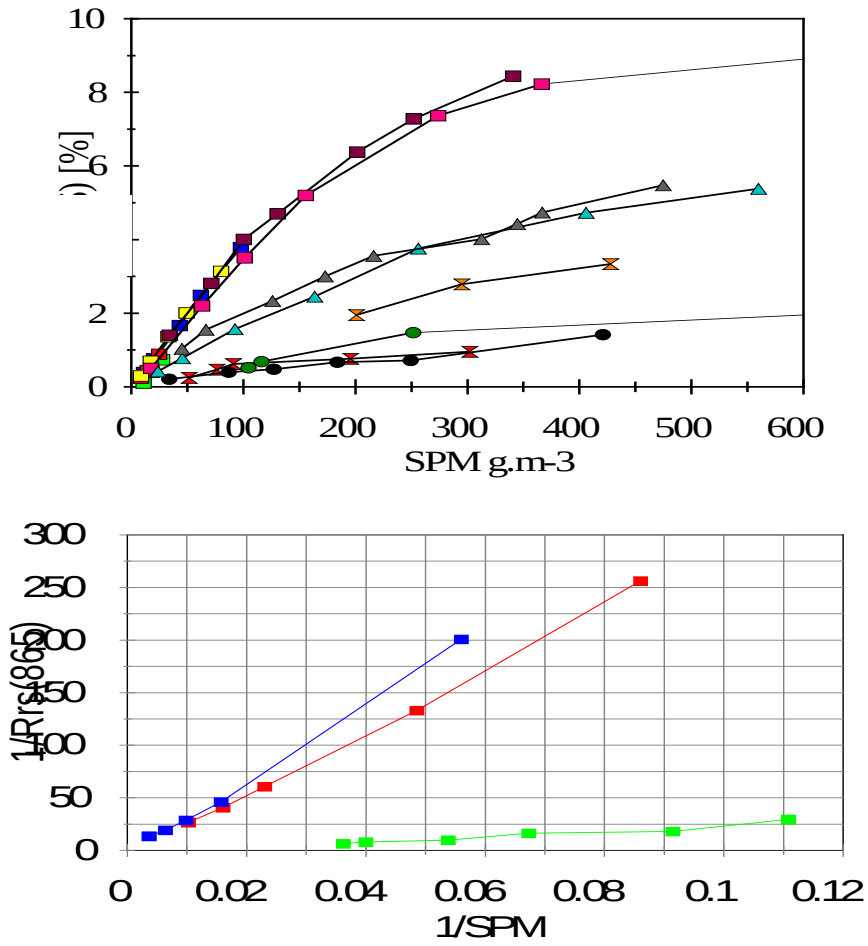

Figure 1: The (a) relationship between suspended sediment and reflectance and (b) relationship between the reciprocals of suspended sediment and reflectance. Data taken from Lavender (2006).

If a fixed viewing geometry and wind speed are chosen the (1a) and (1b) can be expressed as:

$$\rho_w = F\left(\frac{bb_w + bb_p}{a_w + a_p}\right) \tag{3a}$$

$$\rho_w = F'\left(\frac{bb_w + bb_p}{a_w + a_p + bb_w + bb_p}\right) \tag{3b}$$

F and F' are functions that include the terms Q, $\Re$ and π and imply geometry. Both bb/a and $bb/(a+bb)$ are variants of the f factor have been used in a hydro-optical modelling with the latter preferred for case 2 waters.

As the BPAC aims to include waters with very high turbidities and thus reflectances. The limiting values for these alternative reflectance expressions are important in terms of numerical stability. For a non or very low absorbing sediment, such as coccoliths, the limits are:

$$\lim_{bb_{pds}\to\infty} F\left(\frac{bb_w+bb_p}{a_w+a_p}\right)=\infty \quad \text{and} \quad \lim_{bb_{pds}\to\infty} F'\left(\frac{bb_w+bb_p}{a_w+a_p+bb_w+bb_p}\right)=F' \qquad (4a,b)$$

Thus, the $bb/(a+bb)$ variant is more useable since it provides a defined limiting reflectance of F' for high reflectance waters, which can be used as an error check for computing look-up tables (LUT's) and for their implementation.

The limit for absorbing sediment is also of interest. Here, a^*_{bb} is defined as the specific absorption of the sediment backscatter, or the absorption to backscatter ratio, for a particular sediment and in this case (3b) becomes:

$$\rho_w = F'\left(\frac{bb_w+bb_p}{a_w+bb_w+bb_p(1+a^*_{bb})}\right) \qquad (5)$$

And the limiting value becomes:

$$\lim_{bb_{pds}\to\infty} F'\left(\frac{bb_w+bb_p}{a_w+bb_w+bb_p(1+a^*_{bb})}\right)=\frac{F'}{(1+a^*_{bb})} \qquad (6)$$

This limit permits the estimation of sediment absorption from above water reflectance in tank experiments and highly turbid water where analytical and i*n-situ* methods may be problematic.

4.1.2 Implementation of the Hydrological Model

The F' values were computed using Hydrolight 3.0 (Mobley, 1995). The refractive index used was as specified in the MERIS RMD (MERIS Reference Model Document (RMD): Third Reprocessing, PO-TN-MEL-GS-0026), as were the phase functions of pure water and particles. The tables were run for four wind speeds (0.25 ms^{-1}, 1.00 ms^{-1}, 2.75 ms^{-1} and 5.00 ms^{-1}) corresponding to sea-state values recorded in MERMAID (MERis MAtchup In-situ Database, http://hermes.acri.fr/mermaid/home/home.php) metadata, and for solar angles (θ_s) of 0, 15, 30,

45 and 60 degrees that encompasses the MERIS useful viewing geometry. θ_v and Δ_Φ are implicit in the Hydrolight runs and the 'quads' were set to give the following viewing geometry:

θ_v = {0,15,30,45,60}

Δ_Φ = {0,15,30,45,60,75,90,105,120,135,150,165,180}

The absorption values were run from a range of a_w values that were below the minimum found in literature, when adjusted for smile and temperature effects, and to the similar greatest value. Thereafter, a log ramp was applied to an absorption value of 30.0 m^{-1}. From the absorption, scattering values were calculated according to a ramp of single scattering albedo (ω) from zero to 0.9999 with the highest density of values at the high ω. In all, for each band around 10,000 table runs were computed according to the number of candidate a_w values. The *f'* determined from the Hydrolight runs was then fitted to η, where:

$$\eta = \frac{bb_w}{bb_w + bb_p} \tag{7}$$

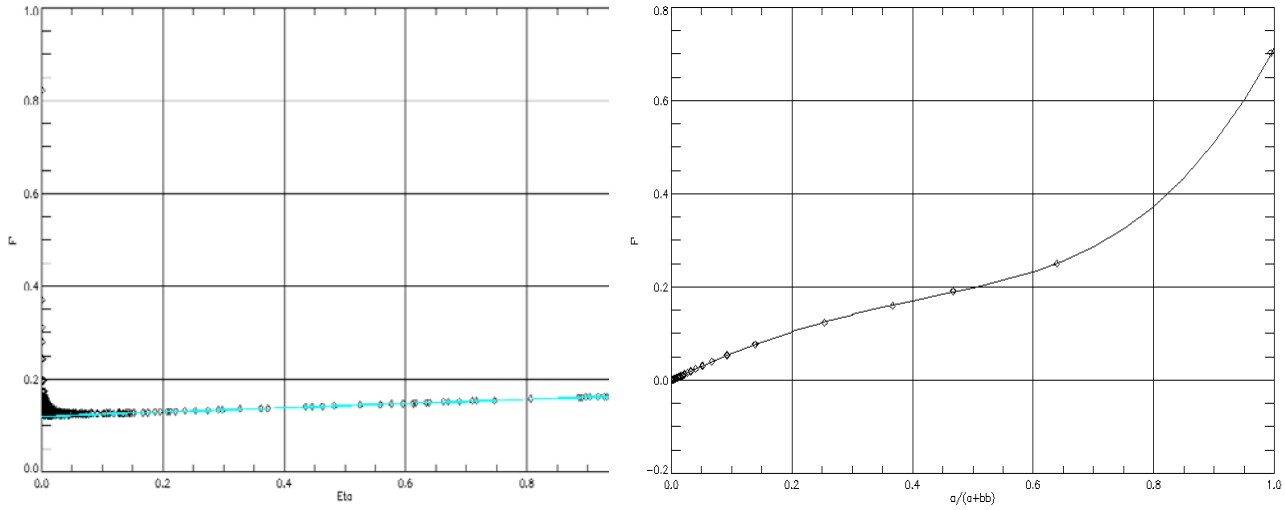

a) Relationship between *F'* and η b) Relationship between *F'* and *bb/(a+bb)*

Figure 2: F' vs. eta and bb/(a+bb)

The relationship with η proved to be linear for low turbidities (Figure 2). The residuals from the fit to η, were expected to relate to ω from previous work on Case I waters (Morel and Gentili, 1993). This however proved unsuccessful, and instead a polynomial relationship was fitted with *F'* being a function of *bb/(a+bb)*.

Thus for any view geometry *F'* can be expressed as:

$$F'=A0+ C.\eta+\sum a_i\{bb/(a+bb)\}^i i \quad (8)$$

where *A0* and *C* are the linear coefficients for η, and $\underline{a_i}$ represents the coefficients of a 4th order polynomial. The *F'* factors are provided as LUTs containing the polynomials for each band, based on wind speed and viewing geometry, with the terms varying slowly so that a simple nearest neighbour lookup is sufficient.

4.1.3 Atmospheric model

For the basic AC the total reflectance at the top of the atmosphere can be written as:

$$\rho_t(\lambda) = \rho_r(\lambda) + \rho_a(\lambda) + \rho_{ra}(\lambda) + \rho_g(\lambda) + t.\rho_w(\lambda) \quad (8)$$

Where $\rho_r(\lambda)$ is the Rayleigh scattering reflectance, $\rho_a(\lambda)$ is the aerosol scattering reflectance, $\rho_{ra}(\lambda)$ is the reflectance resulting from the interaction of $\rho_r(\lambda)$ and $\rho_a(\lambda)$, $\rho_g(\lambda)$ is the sun glitter and t is the diffuse atmospheric transmission. If data are screened for sun glint, the term $\rho_g(\lambda)$ can be ignored. In the CZCS approximation, the term $\rho_{ra}(\lambda)+\rho_a(\lambda)$ can be approximated by the single scattering approximation $\rho_{as}(\lambda)$. Equation (8) thus becomes:

$$\rho_t(\lambda) = \rho_r(\lambda) + \rho_{as}(\lambda)+ t.\rho_w(\lambda) \quad (9)$$

In Case I waters the term $t.\rho_w(\lambda_{NIR})$, NIR water reflectance at the satellite, becomes zero. The term $\rho_r(\lambda_{NIR})$ can be calculated and thus the term $\rho_{as}(\lambda_{NIR})$ determined. Given two wavebands in the NIR it's possible to extrapolate $\rho_{as}(\lambda)$ using either the conventional Angstrom exponent or a variable *c* given in Gordon and Wang (1994). Gordon and Wang (1994) indicated that the *c* extrapolation provides a superior fit for the SeaWiFS bands. In both these cases:

$$\varepsilon_{as}(\lambda_{NIR}(1),\lambda_{NIR}(2)) = \rho_{as}(\lambda_{NIR}(1))/\rho_{as}(\lambda_{NIR}(2)) \quad (10)$$

is used to calculate either *c* or the Angstrom exponent, *n*, where:

$$n = ln[\varepsilon_{as}(\lambda_{NIR}(1),\lambda_{NIR}(2))]/ln[\lambda_{NIR}(1)/\lambda_{NIR}(2)] \quad (11)$$

or

$$c = ln[\varepsilon_{as}(\lambda_{NIR}(1),\lambda_{NIR}(2))]/[\lambda_{NIR}(1)/\lambda_{NIR}(2)] \quad (12)$$

In the case of the Angstrom exponent, $\rho_w(\lambda)$ is calculated as:

$$\rho_w(\lambda) = [\rho_t(\lambda)- \rho_r(\lambda)-\rho_{as}(\lambda_{NIR}(2)).(\lambda/\lambda_{NIR}(2))^n]/t \quad (13)$$

and in the case of *c*, $\rho_w(\lambda)$ is calculated as:

$$\rho_w(\lambda) = \{\rho_t(\lambda)- \rho_r(\lambda)-\rho_{as}(\lambda_{NIR}(2)).exp[c(\lambda/ \lambda_{NIR}(2)]\}/t \quad (14)$$

The transmission can be approximated as:

$$t = exp[-(\tau_r.0.5 + \tau_{oz} + \tau_{wv})/cos(\theta_v)] \quad (15)$$

Where τ_r is the Rayleigh optical thickness, τ_{oz} is the ozone optical thickness, τ_{wv} is the ozone optical thickness and $cos(\theta_v)$ is an approximation of the pathlength. In Case 2 waters, $\rho_w(\lambda_{NIR})$ is no longer zero and the observed $\varepsilon(\lambda_{NIR}(1), \lambda_{NIR}(2))$ becomes:

$$\varepsilon[\lambda_{NIR}(1), \lambda_{NIR}(2)] = \{\rho_{as}[\lambda_{NIR}(1)] + t.\rho_w[\lambda_{NIR}(1)]\} / \{\rho_{as}[\lambda_{NIR}(2)] + t.\rho_w[\lambda_{NIR}(2)]\} \quad (16)$$

This epsilon can be expressed as:

$$\varepsilon[\lambda_{NIR}(1), \lambda_{NIR}(2)] = \varepsilon_{as}[\lambda_{NIR}(1), \lambda_{NIR}(2)] + t.\{\rho_w[\lambda_{NIR}(1)] - \varepsilon[\lambda_{NIR}(1), \lambda_{NIR}(2)].\rho_w[\lambda_{NIR}(1)]\} / \rho_{as}[\lambda_{NIR}(2)] \quad (17)$$

Equation (3) shows that the ratio $\rho_w(\lambda_{NIR}(1))/\rho_w(\lambda_{NIR}(2))$ will always be greater than unity, given $a_w(\lambda_{NIR}(1)) > a_w(\lambda_{NIR}(1))$. If the MERIS NIR bands are used then the value of $\rho_w(\lambda_{NIR}(1))/\rho_w(\lambda_{NIR}(2))$ will be approximately 2, and $\varepsilon[\lambda_{NIR}(1), \lambda_{NIR}(2)]$ will be close to 1. Equation (17) may thus be approximated as:

$$\varepsilon[\lambda_{NIR}(1), \lambda_{NIR}(2)] = \varepsilon_{as}[\lambda_{NIR}(1), \lambda_{NIR}(2)] + 0.5t.\{\rho_w[\lambda_{NIR}(1)]\} / \rho_{as}[\lambda_{NIR}(2)] \quad (18)$$

If the NIR reflectance is not taken into account, equation (18) shows that any NIR water leaving reflectance will result in the observed $\varepsilon(\lambda_{NIR}(1), \lambda_{NIR}(2))$ being greater than the true $\varepsilon_{as}[\lambda_{NIR}(1), \lambda_{NIR}(2)]$. This will result in overestimation of the Angstrom exponent or c parameter in bright pixel waters. The overestimation will then result in an overestimation of the extrapolated $\rho_{as}(\lambda)$ and therefore underestimate or create negative values for the resultant $\rho_w(\lambda)$ with the error being greater at shorter wavelengths. In areas of moderately high particles, where the atmospheric correction does not actually fail (negative $\rho_w(\lambda)$ values), the blue / green ratio will be increased and result in anomalously high retrievals of biogeochemical parameters. In multiple scattering algorithms (e.g. Gordon & Wang, 1994 or Antoine & Morel, 1998) the erroneous estimation of $\varepsilon(\lambda_{NIR}(1), \lambda_{NIR}(2))$ will result in the choice of the incorrect atmosphere model, with similar but less predictable results.

In order to solve this problem in bright pixel waters, it's necessary to solve a coupled hydrological and atmospheric optical model in the NIR (700 - 900 nm) that provides estimates of $\rho_{as}(\lambda)$ that can be used in either a single scattering or multiple scattering model.

It should be noted that in the case of the MERIS atmospheric correction that the Top of Atmosphere (TOA) reflectances are 'pre-corrected' for gaseous absorption, and thus Equation (15) becomes:

$$t = exp[-(\tau_r.0.5)/cos(\theta_v)] \quad (19)$$

4.2 Hydrological Model Parameters

Given the *F'* tables, the BPAC is parameterised entirely using particulate IOPs. The algorithm uses the IOPs of pure water (a_w and bb_w) and particulates (bb_p and a_p) with the final value of bb_p used to estimate TSM for Case 2 flagging and as a potential MERIS product. The model runs used the *F'* polynomial tables, with the parameters as described in this section. A simple atmosphere model is used at the moment with typical values of ρ_{as} taken from MERIS images, and a value of alpha as described. At present no account is taken of the effect of increased surface albedo on the atmospheric path radiance. In terms of the accuracy of the BPAC, the figure of merit is the correct retrieval of the $\rho_w(NIR)$. The TSM product is qualitative since it's a scaled $bb_p(NIR)$ product and the relationship between TSM and $bb_p*(NIR)$ is known to be highly variable; actual sediment concentrations may vary by over +/-50%. Since, in the NIR, there is little difference between the optical properties of phytoplankton, detritus and TSM for Case 1 waters the TSM figures will represent a dry weight or organic material that is closely coupled to chlorophyll concentration.

4.2.1 Pure Water Absorption

Figure 3 shows the absorption of pure water from a number of sources. Although there is good agreement in the 680-700 nm range, there is considerable disagreement at wavelengths greater the 700 nm and especially at the MERIS 775 nm and 865 nm bands. For the BPAC, the final choice of values (Kou et al, 1993) was determined by observed similarity spectra in the NIR (Ruddick et al 2006) from Wetlabs technical reports. In the visible region, the values of Pope and Fry (1997) were chosen. In the region where the Pope and Fry and Kou *et al* values overlapped, the values were combined by giving a weighed window towards the visible for the Pope vales and toward the NIR for the Kou values. Both absorption and error estimates were combined and the full table is supplied in the current MERIS RMD. Both the Kou and Pope values are estimated at a temperature of 22 °C.

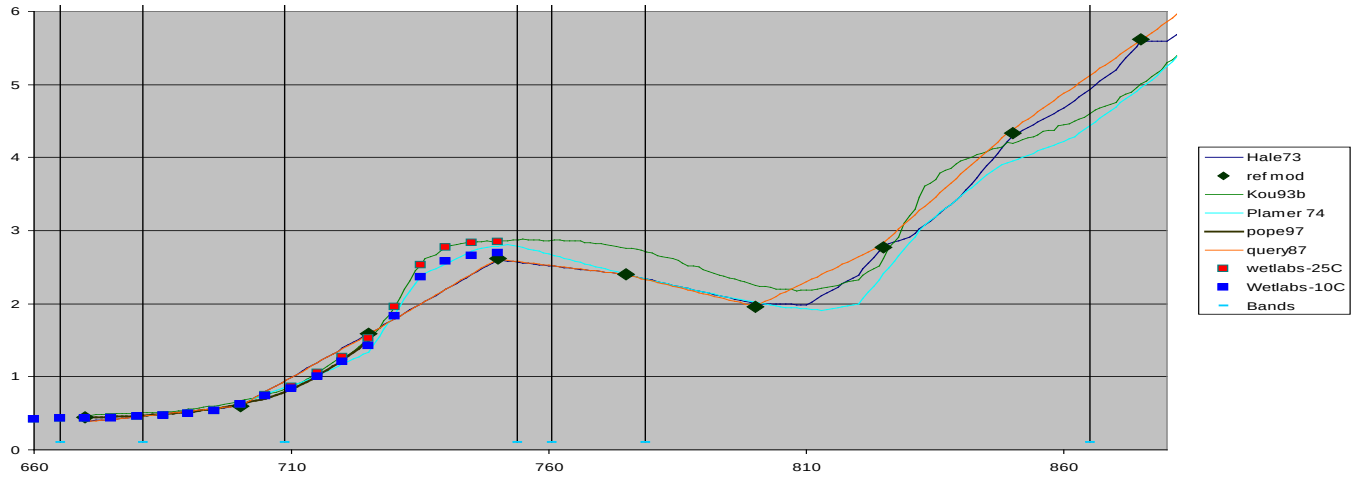

Figure 3: Variation in Water absorption from literature

It should also be noted that both the Kou and Pope absorption values are estimated at a temperature of 22 °C. Temperature effects are more difficult to determine, but Wetlabs provide good figures up to 750 nm and a set of Gaussian decompositions that can enable extrapolation. At wavelengths higher than this there are only brief technical reports. Figure 4 shows one illustration and there are similar data that are in qualitative agreement. In brief, all the NIR bands are to some extent influenced by temperature, but the greatest magnitude is at 753 nm that will make interpretation of data from this band difficult without temperature correction. Preliminary coefficients for the variation of absorption with temperature are provided in the MERIS RMD.

From measures taken by Wetlabs to correct the hyper-spectral AC instrument, salinity effects have been determined and found to be at least an order or magnitude less than temperature effects. They may be influenced by instrument artefacts since it's difficult to discriminate between changes in absorption due to salinity and those caused by changes in the refractive index of water.

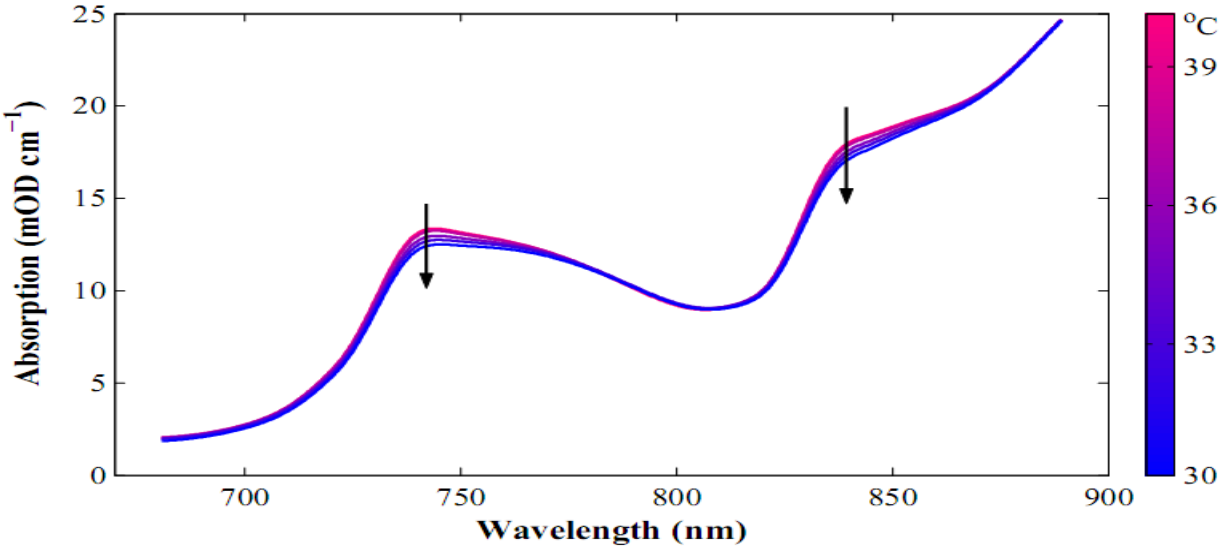

Figure 4: Temperature dependence of water absorption

4.2.2 Pure Water Scattering

The values of pure water backscatter are chosen according to the MERIS RMD for seawater. There is a change in seawater backscatter according to salinity, and sensitivity to this will be examined in a later ATBD release.

This is only expected to affect Case 1 waters and may require flagging in mesotrophic lakes; the current *F'* formulation permits this change of bb_w.

4.2.3 Particulate Absorption

NIR sediment properties at high concentrations are difficult to determine. In order to provide a preliminary set of coefficients to drive the BPAC, the equation for the limiting reflectance described in section 4.1.1 was used on a MERIS image of the Severn estuary. Figure 5 shows a set of points along the Severn estuary against scaled TOA 705 nm reflectance; the image was ICOL processed (code for adjacency correction, http://www.brockmann-consult.de/beam-wiki/download/attachments/13828113/ICOL_ATBD_1.1.pdf) in order to remove any adjacency effects. The data for the points were extracted from MEGS and were Rayleigh and gaseous absorption corrected. The atmosphere was assumed to be homogenous over the area and a simple AC was performed by extrapolating the points to zero reflectance and assuming that this intercept was the true ρ_{as}. The value for alpha was obtained from the Level 2 image for pin 1 and pin2. This ρ_{as} was subtracted from all the pin points and the saturation radiance obtained by fitting a Gompertz curve to Figure 5b. The absorption obtained is given in the MERIS RMD, and showed a weak exponential decline with wavelength.

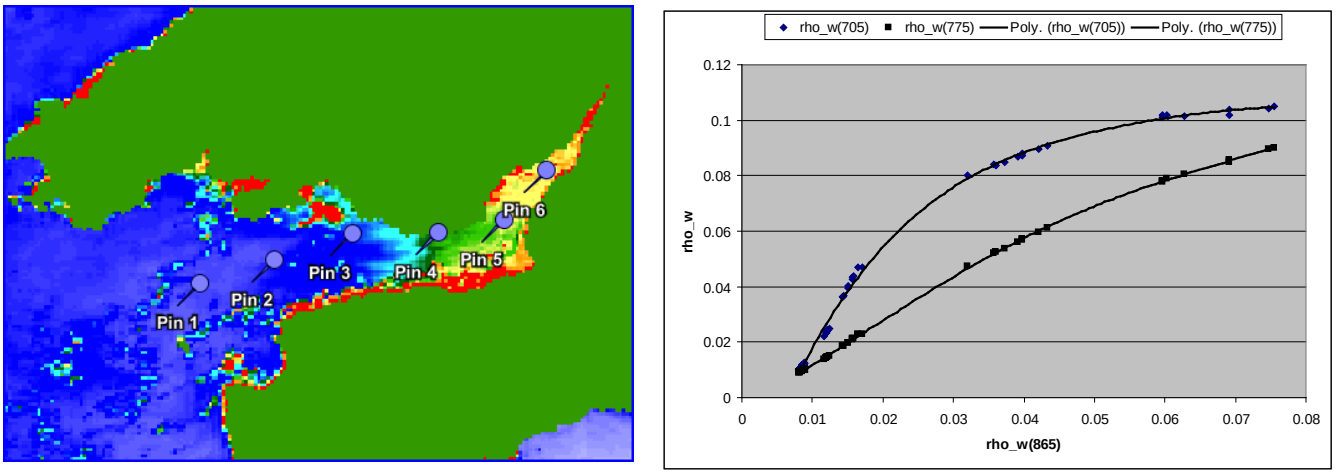

a) Severn estuary pin set b) reflection saturation at the Severn estuary pin set

Figure 5: Reflectance saturation - Severn Estuary

This exercise will be completed on further images and complemented by Mie modelling. Specifically this needs to be done for white scatters.

4.2.4 Particulate Scattering

The present values for particulate scattering are those specified in the MERIS RMD for Case 2 waters. As such, the BPAC is internally consistent with the neural network and protocol values. This is expected to evolve when white scatterers are accounted for as their spectral slope is known to approach 1 rather than the 0.4 as specified in the MERIS RMD.

4.2.5 Chlorophyll Absorbance and Fluorescence

Preliminary data from hyper-spectral radiometer measurements, where there is a strong fluorescence peak, indicate the there is potential contamination of the 705 nm band by the fluorescence signal. However, quantitative analysis of these results awaits an adequate stray-light correction scheme for these instruments. At present we assume that the Gaussian formulation of Gordon (1979) is appropriate.

Figure 6 shows the normalised chlorophyll fluorescence and absorption parameters described in the MERIS RMD. The absorption curve is from Bricaud *et al* (1998) and the fluorescence curve is from the standard Gaussian in the MERIS RMD. Also shown for reference is the shifted absorption curve, since this may better match the chlorophyll fluorescence shown *in vivo*. It can be seen that there is significant overlap at the 705 nm band. The extra reflectance at 705 nm, due to fluorescence rather than particle scattering, results in an overestimate of ρ_w(NIR) and the consequent error in the BPAC.

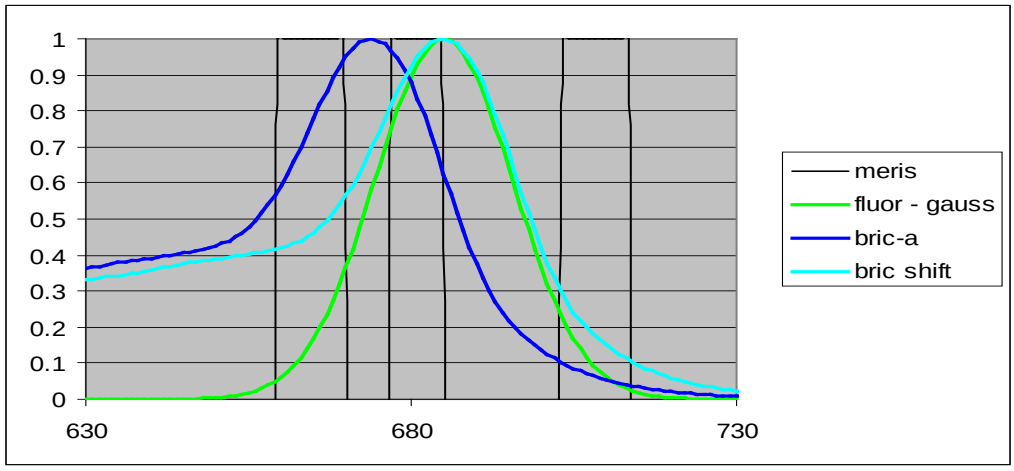

Figure 6: Chlorophyll fluorescence and absorption for MERIS Bands

The effect can be corrected by using the first estimate of $bb_p(705)$ derived in section 4.4.8; the BPAC low band set solution. It's assumed that there is no fluorescence and thus the corrected reflectance $\rho'_w(\lambda)$ is equal to $\rho_w(\lambda)$ and that initally $a_p(670)$ is zero. The solution is iterated until the relative change in $\rho_f(685)$ is less than 0.01%. If $\rho_f(685)$ <= 0 then the calculation is terminated since fluorescence correction is unnecessary. The $bb_p(705)$ estimated from the fluorescence corrected reflectance is then returned to the BPAC. The iterative procedure typically takes around 5 iterations.

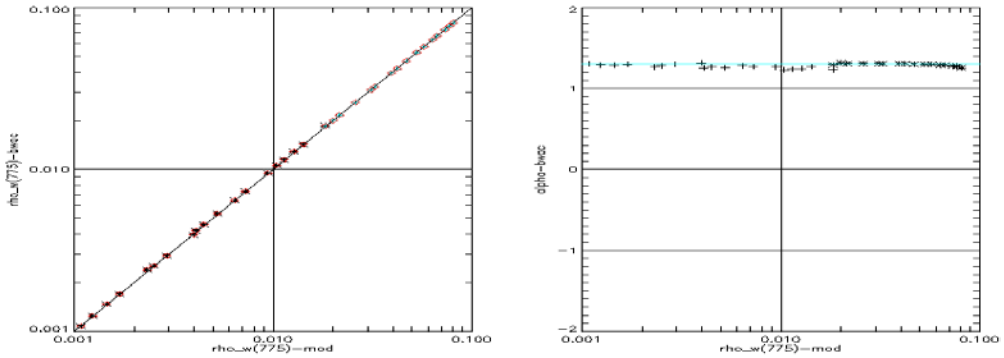

a) The nominal BPAC Correction – without natural fluorescence

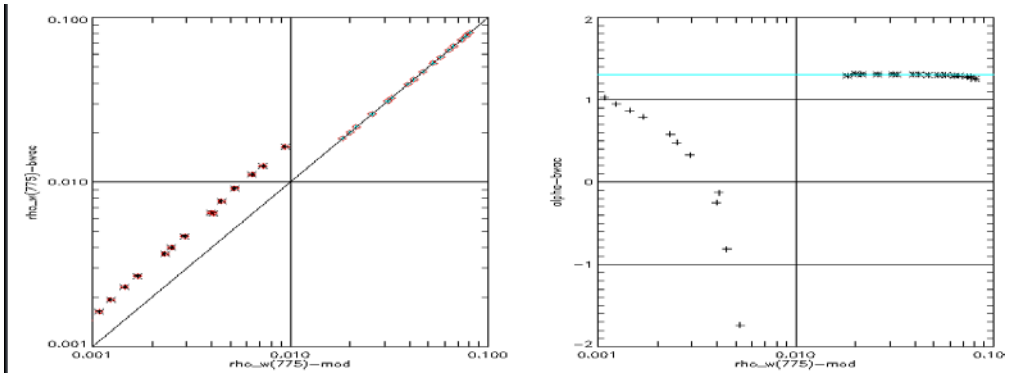

b) The nominal BPAC Correction – with natural fluorescence

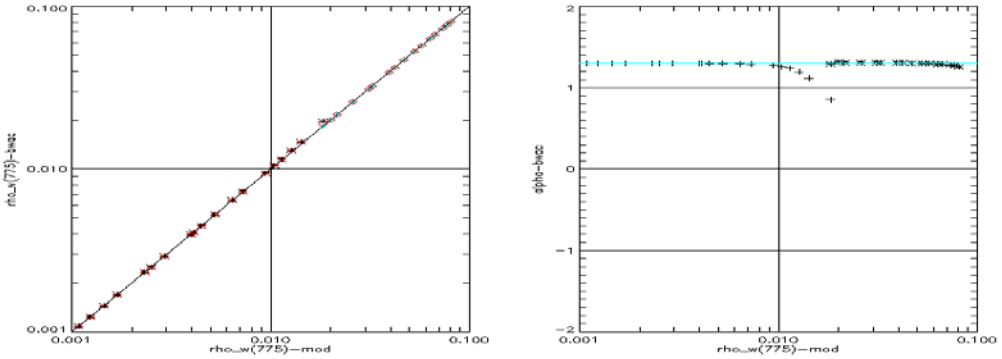

c) The BPAC Correction – with the fluorescence corrections and natural fluorescence

Figure 7: Effects of natural fluorescence on BPAC

$a_p(670)$ is estimated as follows:

$$bb_p(670)=bb_p^*(670).bb_p(705)/bb_p^*(705) \quad \text{(F1)}$$

$$a(670)= a_p(670)+a_w'(670)+ bb_p(670).\ a_{bb}^*(670) \quad \text{(F2)}$$

$$F'=F'(670,\ \theta v,\theta s,\Delta\Phi,a(670),bb_w(670),bb_p(670)) \quad \text{(F3)}$$

$$a_p(670)=[bb_p(670)+bb_w(670)].[F'/\rho'_w(670)-1]-a_w'(670)- bb_p(670).\ a_{bb}^*(670) \quad \text{(F4)}$$

$\rho'_w(685)$ is estimated as follows:

$$bb_p(685)=bb_p^*(685).bb_p(705)/bb_p^*(705) \quad \text{(F5)}$$

$$a_p(685)=a^*_p(685).a_p(670)/a^*_p(670) \quad \text{(F6)}$$

$$a(685)=a_w'(685)+a_p(685)+bb_p(685).\ a_{bb}^*(685) \quad \text{(F7)}$$

$$F'=F'(685,\ \theta_v,\theta_s,\Delta_\Phi,a(685),bb_w(685),bb_p(685)) \quad \text{(F8)}$$

$$\rho'_w(685)=F'.[bb_p(685)+bb_w(685)]/[bb_p(685)+bb_w(685)+a(685)] \quad \text{(F9)}$$

The fluorescence is estimate as follows, assuming $K(\lambda)\approx a(\lambda)$:

$$\rho_f(685)= \rho_w(685)- \rho'_w(685) \quad \text{(F10)}$$

$$\rho_f(\lambda)= \rho_f(685).Lfn(\lambda).E0(685).a(685)/ Lfn(685).E0(\lambda).a(\lambda) \quad \text{(F11)}$$

where $Lfn(\lambda)$ is the normalised fluorescence spectra derived from the Gaussian, and since $E0(\lambda)$.is a constant, the fluorescence spectrum that is adjusted for $E0(\lambda)$, $\rho fn(\lambda)$ can be used.

The fluorescence corrected reflectance $\rho'_w(\lambda)$ is derived as:

$$\rho'_w(\lambda)= \rho_w(\lambda)- \rho_f(\lambda) \quad \text{(F12)}$$

From this a new estimate of $bb_p(705)$ is calculated according to section 4.4.7 and iteration resumes at (F1).

Table 1 shows provisional values for the relative fluorescence height and for the chlorophyll specific absorption.

Band (nm)	*Lfn(λ)*	*ρfn(λ)*	$a_p(\lambda)$
670	0.1884	0.1810	0.3129
685	0.9135	0.9135	0.2053
709	0.1448	0.1514	0.0176

Table 1: Fluorescence height and phytoplankton absorption

4.3 Model Sensitivity

4.3.1 Similarity and Optimal Band Choice

Figure 8 shows the expected similarity spectrum derived from the hydro-optical model, together with the expected ratios for an alpha of 0.5 and 1.5. For all the band pairs it can be seen that there are no problems discriminating between the slope of path radiance and the slope of water reflectance up to a nominal TSM value of around 500 $g.m^{-3}$, although the actual in *in situ* gravimetric values may be as low as 100 $g.m^{-3}$. The problem is using the 705 nm band for the variable sediment absorption.

Figure 8d shows the hydro-optical model run for an absorbing and non-absorbing sediment. There is a clear change in the ratio between the absorbing and non-absorbing reflectance at concentrations greater than 10 $g.m^{-3}$, and although the studies on the Severn estuary (see section 4.2.3) can to some extent account for this, a method needs to be developed to estimate sediment absorption from images; perhaps using the 412nm band. The solution for the problems with the 705 nm band set is to use higher band set for TSM >10 $g.m^{-3}$. For these higher concentrations the 775, 865,885 nm band set can be used. Figure 9 shows the similarity for the 885 nm band. The 865:885 band pair shows no overlap between aerosol properties for nominal concentrations >1000 $g.m^{-3}$, and thus is the optimal band pair for estimating alpha. In contrast, the 775:885 band pair is optimal and can be used to estimate ρ_{as} given an alpha estimate.

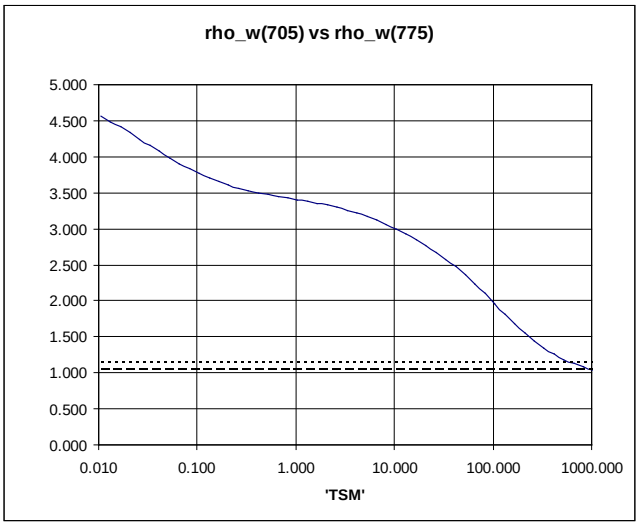

a) Similarity spectrum for 705 vs. 775

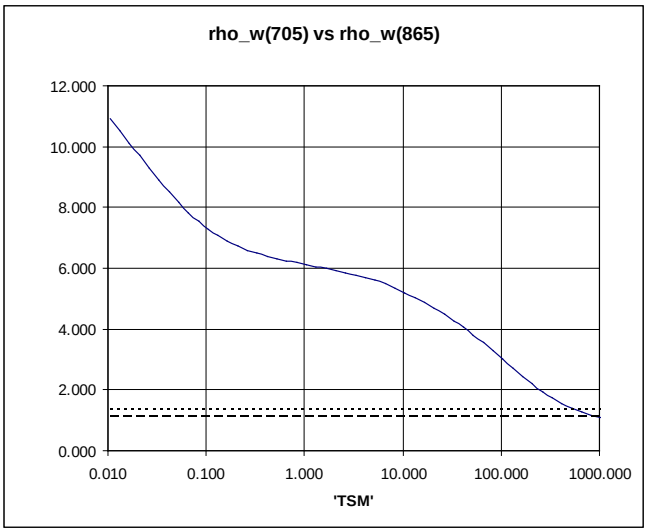

b) Similarity spectrum for 705 vs. 865

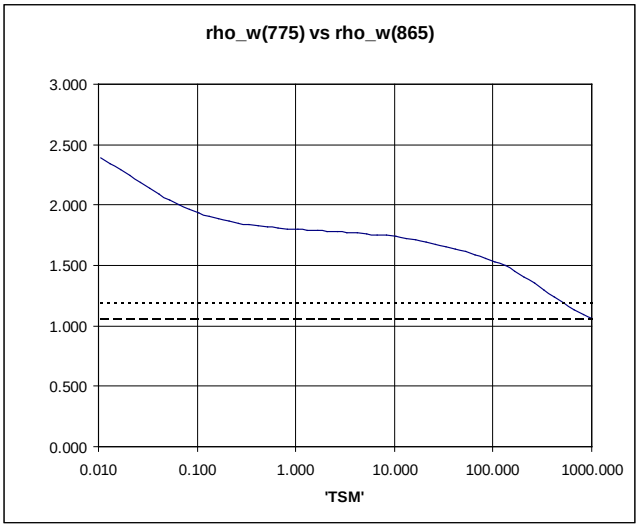

c) Similarity spectrum for 775 vs. 865

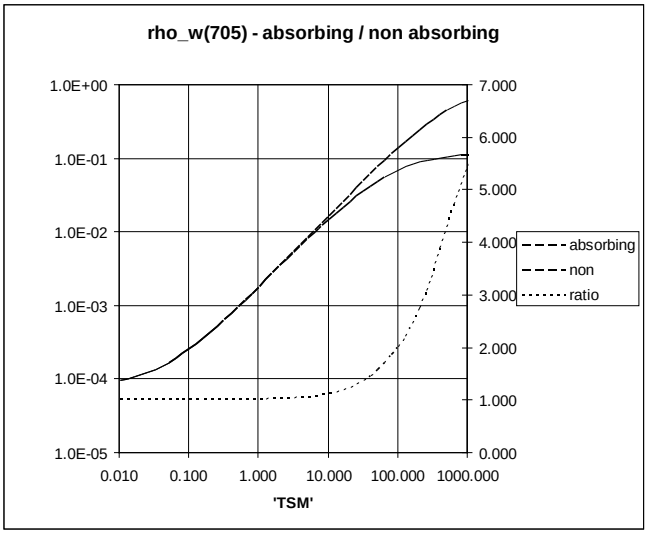

d) Modelled absorbing / non absorbing sediments

Figure 8: Similarity spectrum for low band set

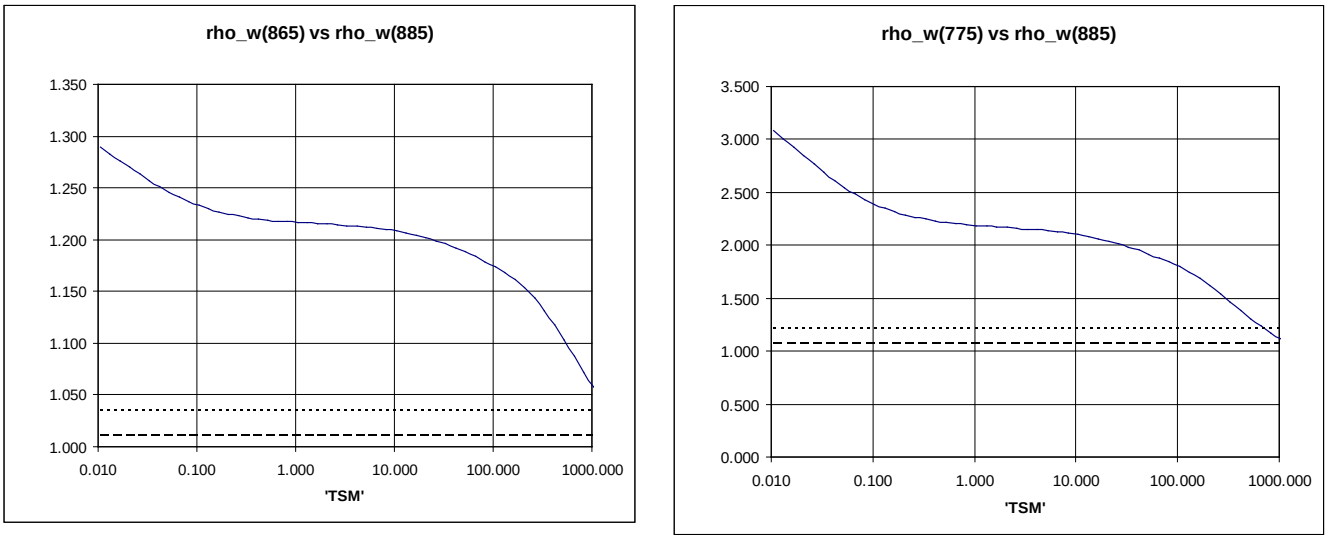

a) Similarity spectrum for 865 vs 885 b) Similarity spectrum for 776 vs 885.

Figure 9: Similarity spectrum for high band set

4.3.2 Temperature and Smile

Figure 10 shows the effect of the change in the absorption coefficient of pure water on the low band set BPAC retrieval (see section 4.3.1 for information on the band set). The input a_w is adjusted for the temperature and the BPAC is run at the nominal values. The nominal alpha for the simulated data is 1.3, and it can be seen that there is a strong error in the retrieved alpha with an underestimate at TSM concentrations of >2g.m^{-3}. The error in the alpha nominal at TSM >12g.m^{-3} is due to the errors implicit in using the lower band set. The result of this underestimate is to produce negative estimates of ρ_w at visible wavelengths.

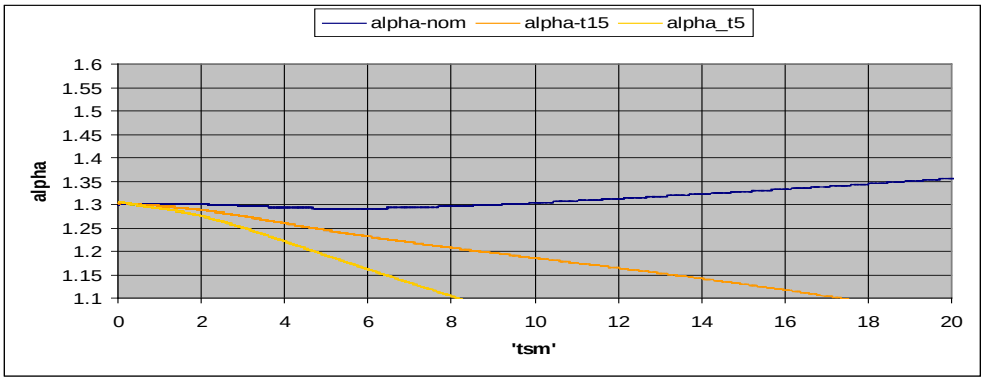

Figure 10: Sensitivity to Temperature - low band set

Figure 11 shows the effect of smile on the low band BPAC; as for Figure 10, but with the input a_w shifted by 1 nm. The smile change results in a dramatic error in the retrieved alpha at TSM concentrations of >2 g.m^{-3}. This error would result in the MERIS AC being unable to determine a suitable candidate aerosol, and atmospheric correction failure.

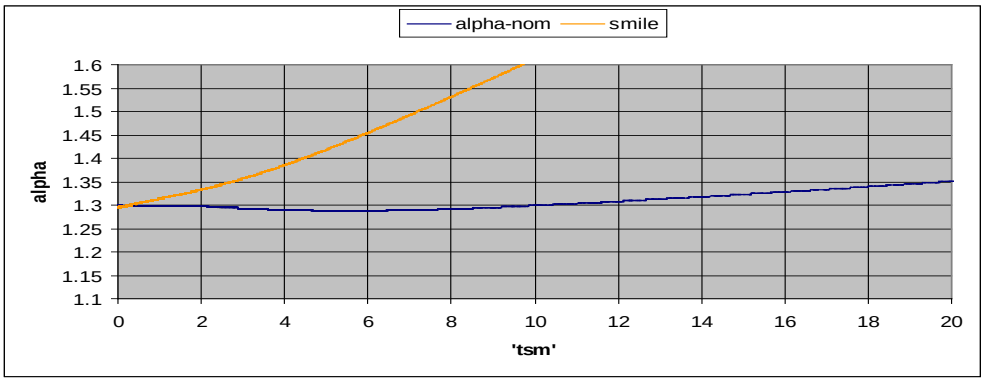

Figure 11: Sensitivity to 1 nm smile low band set

4.3.3 MERIS radiometric sensitivity and Aerosol retrieval error

During the evolutions of the BPAC there has been some debate about the appropriate threshold at which to run the BPAC correction. This threshold is not related to the water type, i.e. Case 1 / Case 2, rather it's related to the absolute backscatter in the NIR and it detectability by MERIS. Figure 12 shows the number of MERIS counts for the BPAC bands associated with nominal TSM, at solar zenith angles of 30 and 60 degrees. It can be seen that the effects of particulate scattering are detectable below 0.01 mg.m^{-3} in the 705 nm band. However, in order to successfully run the BPAC around 0.3 – 0.5 mg.m^{-3} of TSM are required for the low band set, and 0.7 – 1.0 mg.m^{-3} of TSM are required for the high band set. These thresholds are geometry dependant. The suggested threshold for 705 nm is 10 counts, but needs to be validated in terms of any image artefacts.

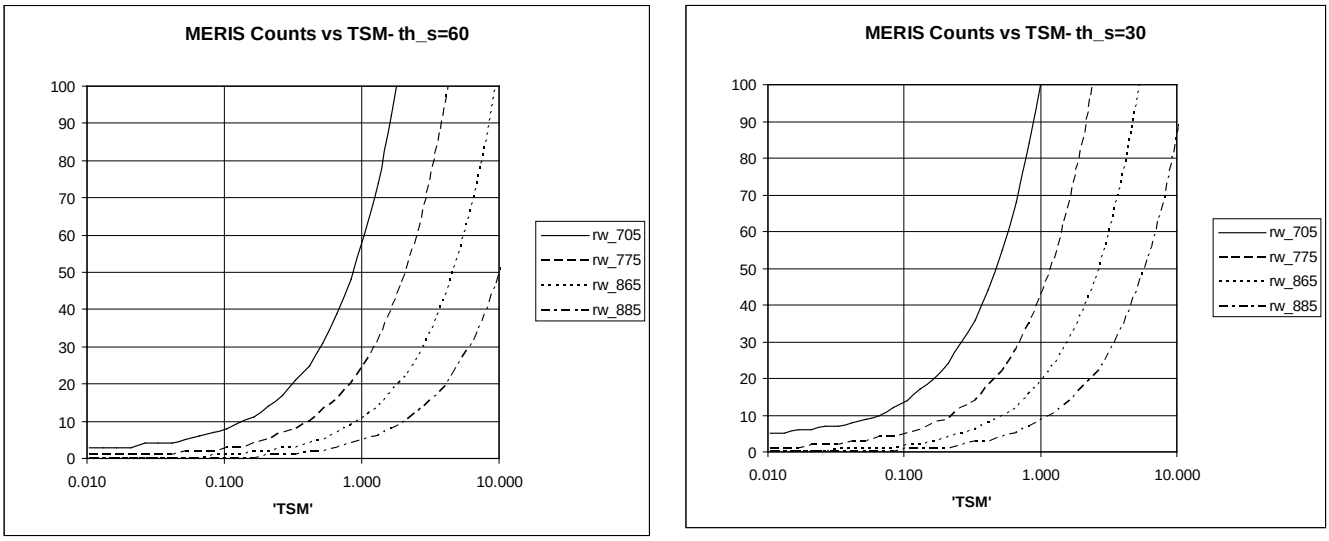

a) MERIS Counts vs. TSM at sun zenith of 60 degrees b) MERIS Counts vs. TSM at sun zenith of 30 degrees

Figure 12: MERIS Counts vs. sediment load

Figure 13a shows the error in the estimation of alpha (α) by the BPAC for two values of α(0.5,1.5) and two values of $\rho_{as}(705)$ (0.005,0.02) in terms of MERIS counts at 865nm. In terms of errors, there is an interaction between ρ_{as} and α; however, the highest error is for a low α and a low turbidity atmosphere. In terms of a single scattering, with CZCS type AC, these errors do not propagate to high errors in the estimated $\rho_{as}(412)$, Figure 13b. However, the effects on the MERIS AC are less predictable since the NIR α is used to choose the aerosol model. These preliminary results indicate a sensitivity of the BPAC to aerosols needs to be investigated using the full MERIS AC.

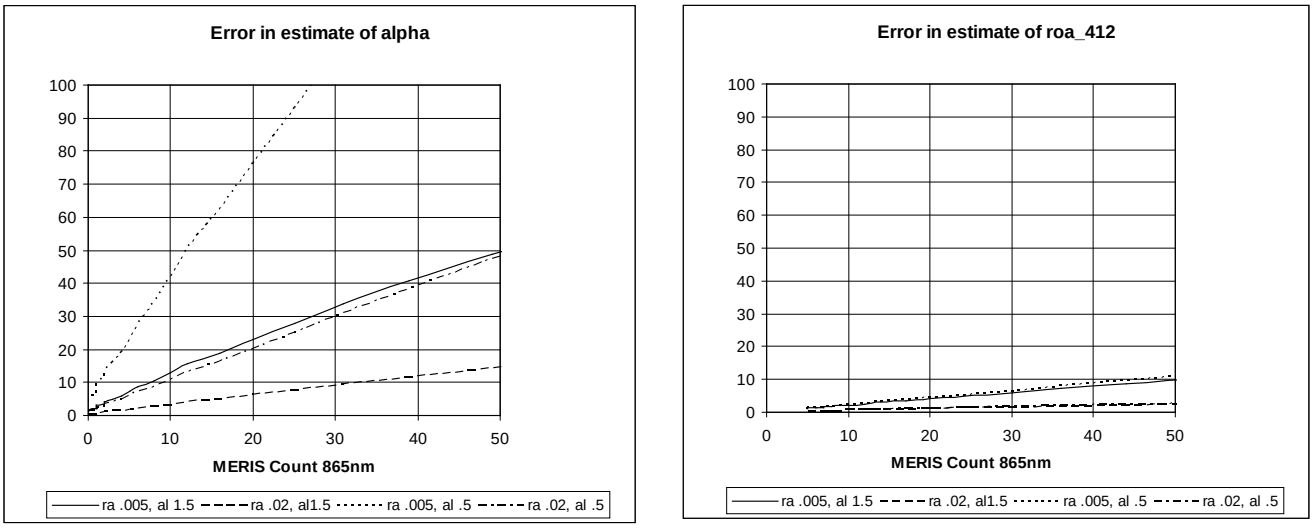

a) α error vs. MERIS counts b) $\rho_{as}(412)$ error vs. MERIS Counts

Figure 13: Aerosol retrieval errors vs. MERIS Counts

4.4 Implementation

Compared to the original implementation of the BPAC (e.g. Lavender *et al.* 2005) where TSM was used as a state variable, the model is implemented in terms of the IOPs and the parameterisation as described in the previous sections. The solution relies of providing estimates from a low band set {705nm, 775nm, 865nm} and a high band set {775nm, 865nm, 885nm}. For the initial estimates, the first two wavelengths of the band sets are used.

4.4.1 Rayleigh correction

In the MERIS processor the reflectance is pre corrected for glint (i.e. where either no glint or the medium glint flags is asserted) and gaseous absorption, and thus the following quantity is calculated from the glint and absorption corrected $\rho_t(\lambda)$:

$$\rho_{rc}(\lambda) = \rho_t(\lambda) - \rho_r(\lambda) \quad \text{(S1)}$$

Note the $\rho_t(\lambda)$ – different to that described in atmospheric model.

4.4.2 Temperature and Smile Offsets

$$a_w'(\lambda') = a_w(\lambda) + K\lambda a*(\lambda - \lambda') + KTa*(22.0 - T) \quad \text{(S2)}$$

Where λ is the nominal wavelength of the standard water absorption, λ' is the actual MERIS wavelength and $K\lambda a$ is the rate of change of water absorption with wavelength; T is the observed temperature, 22.0 is the standard

laboratory temperature for which the tables are provided and *KTa* is the rate of change of absorption with temperature. At present it is assumed that there is no interaction between $K\lambda a$ and *KTa*. It is also assumed that bb_w, bb_p, a_p have low sensitivities relative to wavelength.

4.4.3 Choice of IOPs

Although white scatterers such a coccolithophores rarely have saturation reflectance at they have significantly different scattering properties, since they do not have the levels of associated CDOM.

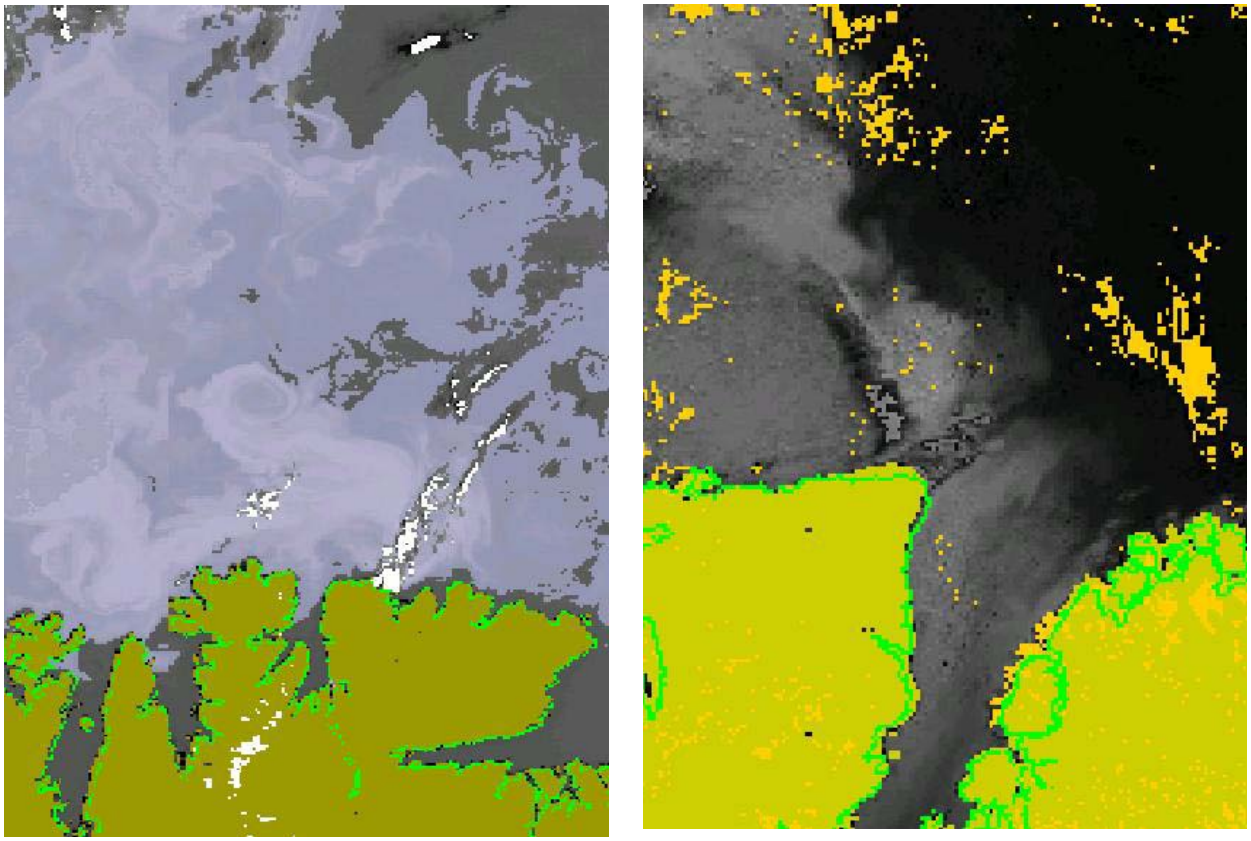

a) Barents sea coccolithophores bloom b) Amazon Plume

Figure 14: White scatter Flag

The white scatterers are detected by a simple TOA log ratio flag and threshold:

The flag is:

$$ln\{[t_d(709)/t_d(620)][\rho_{rc}(620).a_w(620)]/[\rho_{rc}(709).a_w(709)]\}/ln\{620/709\}$$

The current flag threshold is 4.8. Figure 14 shows a comparison of the flag output for highly reflective coccolithophore bloom in the Barents Sea (a) compared with a highly reflective scene over the Amazon plume (b). The assertion of the flag is shown as purple in the Barents. It can be seen that the flag is not asserted in the coastal waters of the Barents sea and never asserted in the Amazon plume. Figure 11 shows the comparative 709/781 similarity slope for two scattering areas, the Barents Sea and the Severn estuary. Although the data range is different, the coccolithophores maintain a linear slope up to a $\rho_{rc}(709)$ of 0.02. This reflectance range will also encompass whitecaps and bubbles.

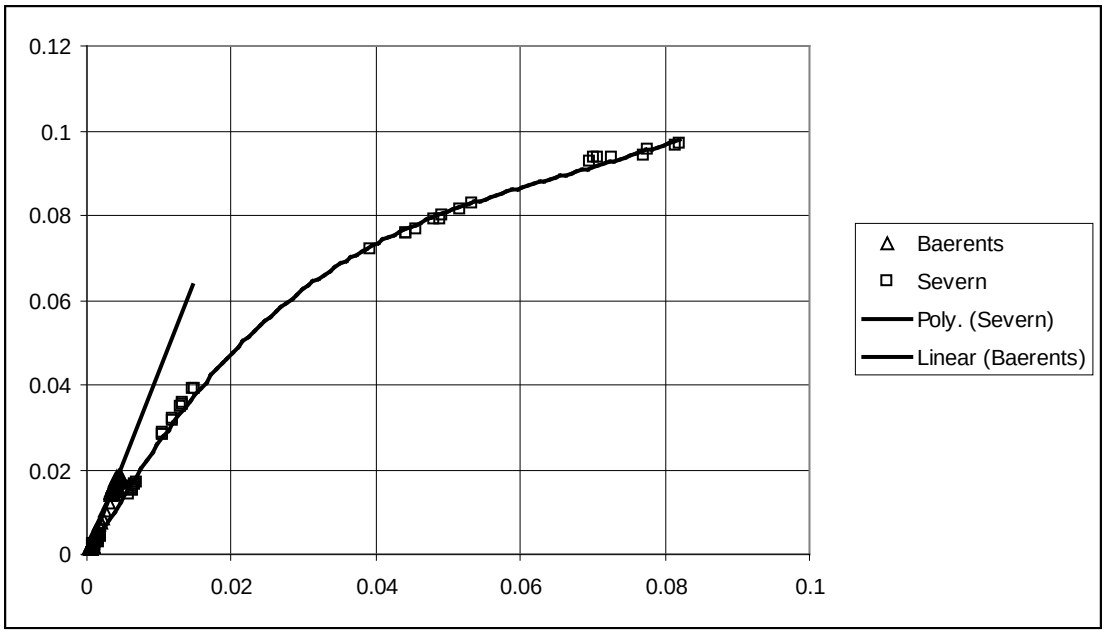

Figure 15: Comparative scattering in Severn Estuary and Barents Sea

4.4.4 Initial Estimates

The atmospheric path reflectance in the NIR can be solved simply if an angstrom exponent is known and the shape of the water reflectance is known. The solution can be defined in terms of *Kw*, the TOA ratio of water reflectance at two bands (λ_1, λ_2), and *Ka* the ratio of path radiance, related to the angstrom exponent, but other atmosphere models could be used. The ratios are defined as:

$$Kw = [\rho_w(\lambda_2)*t(\lambda_2)]/[\rho_w(\lambda_1)* t(\lambda_1)] \quad (I1)$$

$$Ka = (\lambda_2/\lambda_1)^{\wedge}\alpha \quad (I2)$$

$$\rho_w(\lambda)=F'(\lambda, \theta_v,\theta_s,\Delta\Phi,a(\lambda),bb_w(\lambda),bb_p(\lambda))*a(\lambda)/[a(\lambda)+bb_p(\lambda)+bb_w(\lambda)] \quad \text{(I3)}$$

$$a(\lambda)= a_w'(\lambda')+ a^*_{bb}(\lambda)*bb_p(\lambda) \quad \text{(I4)}$$

From (S5) and (S6) it can be seen that *Kw* is dependent on *F'* and $bb_p(\lambda)$. For the low band estimate, $bb_p(775)$ is set to 0.001 and for the high band estimates $bb_p(775)$ is set to 0.5; both compatible with Case 1 waters. At the other wavelengths $bb_p(\lambda)$ is determined from $bb_p*(\lambda)$.

Given *Kw* and *Ka* it is possible to determine $\rho_{as}(\lambda)$, from a simple difference equation:

$$\rho_{as}(\lambda_1)=(\rho_{rc}(\lambda 1)-Kw*\rho_{rc}(\lambda 2))/(Ka-Kw) \quad \text{(I5)}$$

In terms of practical implementation it should be noted that when $Ka \approx Kw$, then the $\rho_{as}(\lambda_1)$ is undefined, since the atmospheric and water reflectance are identical. The water reflectance is simply estimated as:

$$\rho_w(\lambda_1)=(\rho_{rc}(\lambda_1)- \rho_{as}(\lambda_1))/t(\lambda_1) \quad \text{(I6)}$$

4.4.5 Band Choice

Figure 16a show the relationship between TSM and the ratio of the true value of $\rho_w(775)$ and the initial estimate of $\rho_w(775)$. The setting of the initial values of $bb_p(775)$ gives mild overestimates for the low band estimates up to a value of around 10 mg.m^{-3} and matching underestimates for the high band estimate; this crossover point matches the applicability of the two iterative procedures and Figure 16b shows the corresponding reflectance estimates. The band choice is based on the high band estimate, since at high turbidities the low band estimate may become zero and is potentially affected by errors in the estimation of water vapour absorption.

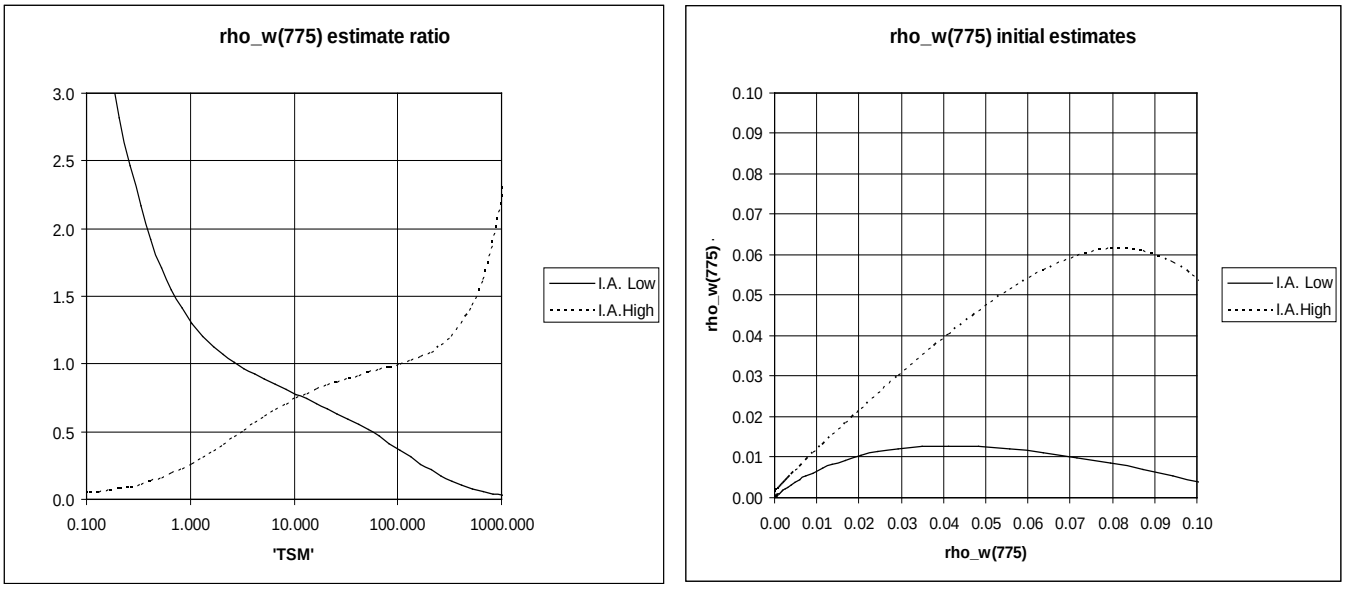

a) Initial estimates vs. Nominal TSM b) actual and initial estimates of $\rho_w(775)$

Figure 16: BPAC Initial Estimates

The current thresholds are:

$\rho_w(775)<0.15$ → Use low band set only

$\rho_w(775)>0.02$ → Use high band set only

The level of overlap is chosen for computational efficiency and could be broadened.

4.4.6 Radiometric Thresholding

The threshold is based on the number of MERIS counts, and on the low band $\rho_w(705)$ estimate. The test is only applied when the high band estimate is less than 0.15, since depending of the sediment absorption at high turbidities the $\rho_w(705)$ may be zero or negative.

The threshold is calculated as:

$$min\_\rho_w(705)=\pi*[n\_bit\_705.mean\_gain(705)]/[e0(705).\cos(\theta_S)]/\ t_d(705) \quad \text{(S2)}$$

where *mean_gain(705)* is the average gain over all the cameras, *e0(705)* is the TOA solar irradiance and *n_bit_705* is the desired threshold in MERIS counts. Both *mean_gain(705)* and *e0(705)* should be in the same radiometric units.

4.4.7 Determination of bb from $\rho_w(\lambda)$

The determination of bb_p as a function of $\rho_w(\lambda)$ is non trivial in computational terms and is required for both the high and low band estimates.

Given:

$$\rho_w(\lambda)=F.\ a(\lambda)/[a(\lambda)+bb_w(\lambda)+bb_p(\lambda)] \quad \text{(S3)}$$

bb_p can be inverted as :

$$bb_p(\lambda)=[\rho_w(\lambda).a(\lambda)]/[F'-\rho_w(\lambda)]-bb_w(\lambda) \quad \text{(S4)}$$

In Case 1 waters this does not present a problem since $\rho_w(\lambda)<<F'$, and the can be iterated since $a(\lambda)=aw'(\lambda')+a^*_{bb}(\lambda)*bb_p(\lambda)$, convergence is simple achieved using $\Delta bb_p(\lambda)$ as a convergence criteria.

Highly turbid Case 2 waters present a problem, since $\rho_w(\lambda)$ can be > or equal F', as a result there is either an arithmetic error, where the denominator above becomes zero or a negative $bb_p(\lambda)$ is determined. In this case an estimate of $bb_p(\lambda)$ is obtained F, where:

$$F=F'.a(\lambda)/[a(\lambda)+bb(\lambda)+bb_w(\lambda)] \quad \text{(S5)}$$

and:

$$bb_p(\lambda)=[\rho_w(\lambda).a(\lambda)]/F-bb_w(\lambda) \quad \text{(S6)}$$

This is iterated using the above relationship for $a(\lambda)$, and convergence is achieved when $F'>\rho_w(\lambda)$. Thereafter, the Case 1 iterative method is used.

4.4.8 Low Band Solution

The iterative solution is initialised with an alpha and $\rho_w(705)$ from the initial estimates above. $bb_p(705)$ is calculated according to section 4.4.7. Optionally this estimated is corrected for the natural fluorescence of chlorophyll described in section 4.2.5. Convergence is based of the relative error of the estimated *bb*:

$$\text{abs}(bbp_{\text{iter-1}} - bbp_{\text{iter}})/bbp_{\text{iter}} < \text{tol} \quad \text{(L1)}$$

the tolerance is around 0.001, and the BPAC fails if iter>30. The $bb_p(705)$ estimated at this point can be optionally corrected for errors due to natural fluorescence. From the new estimate of $bb_p(705)$ - $\rho_w(775)$, $\rho_w(865)$ are calculated according to the IOPs:

$$bb_p(\lambda)=bb_p^*(\lambda).bb_p(705)/bb_p^*(705) \quad \text{(L2)}$$

$$a(\lambda)= aw'(\lambda')+ a^*_{bb}(\lambda)*bb_p(\lambda) \quad \text{(L3)}$$

$$\rho_w(\lambda)=F'(\lambda, \theta_v,\theta_s,\Delta_\Phi,a(\lambda),bb_w(\lambda),bb_p(\lambda))*a(\lambda)/[a(\lambda)+bb_p(\lambda)+bb_w(\lambda)] \quad \text{(L4)}$$

The estimated $\rho_{as}(\lambda)$ is determined as:

$$\rho_{as}(\lambda)=\rho_{rc}(\lambda)- \rho_w(\lambda).t(\lambda) \quad \text{(L5)}$$

If either of these $\rho_{as}(\lambda)$ are <= to zero then this is treated as an exception and the BPAC has failed. The alpha corresponding to the $\rho_{as}(\lambda)$ is calculated as:

$$\alpha=\ln(\rho_{as}(775)/ \rho_{as}(865))/ln(775/865) \quad \text{(L6)}$$

Optionally the value of α can be constrained at this stage such that $\rho_{as}(412)<= \rho_{rc}(412)$. The difference equation in section 4.4.4 is used to determine $\rho_{as}(705)$, where *Kw* and *Ka* are:

$$Kw= [\rho_w(775)*t(775)]/[\rho_w(705)* t(705)] \quad \text{(L7)}$$

$$Ka=(775/705)^\alpha \quad \text{(L8)}$$

A new estimate of $\rho_w(705)$ is obtained from the $\rho_{as}(705)$ estimated by the difference equation as:

$$\rho_w(705)= (\rho_{rc}(705)- \rho_w(705))/t(705) \quad \text{(L9)}$$

An estimate of $\rho_w(705)$ <= zero is treated as an exception and the BPAC fails. The procedure then proceeds to the next iteration. On successful completion $\rho_w(775,865,885)$ are calculated according to (L2,L3,L3) and $bb_p(775)$ is preserved in order to estimate TSM.

4.4.9 High Band Solution

The iterative solution is initialised with an alpha and $\rho_w(865)$ from the initial estimates above. $bb_p(865)$ is calculated according to section 4.4.7. Convergence is based of the relative error of the estimated *bb*:

$$\text{abs}(bbp_{iter-1} - bbp_{iter})/bbp_{iter} < tol \quad \text{(H1)}$$

The tolerance is around 0.001, and the BPAC fails if iter>60. From the new estimate of *bbp(865)* - $\rho_w(775)$, $\rho_w(885)$ are calculated according to the IOPs:

$$bb_p(\lambda)=bb_p^*(\lambda).bb_p(705)/bb_p^*(705) \quad \text{(H2)}$$

$$a(\lambda)= aw'(\lambda')+ a_{bb}^*(\lambda)*bb_p(\lambda) \quad \text{(H3)}$$

$$\rho_w(\lambda)=F'(\lambda, \theta_v,\theta_s,\Delta\Phi,a(\lambda),bb_w(\lambda),bb_p(\lambda))*a(\lambda)/[a(\lambda)+bb_p(\lambda)+bb_w(\lambda)] \quad \text{(H4)}$$

The estimated $\rho_{as}(\lambda)$ is determined as:

$$\rho_{as}(\lambda)=\rho_{rc}(\lambda)- \rho_w(\lambda).t(\lambda) \quad \text{(H5)}$$

If either of these $\rho_{as}(\lambda)$ are <= to zero then this is treated as an exception and the BPAC has failed. The alpha corresponding to the $\rho_{as}(\lambda)$ is calculated as:

$$\alpha=\ln(\rho_{as}(775)/ \rho_{as}(865))/\ln(775/865) \quad \text{(H6)}$$

Optionally the value of α can be constrained at this stage such that $\rho_{as}(412)<= \rho_{rc}(412)$.The difference equation in 4.4.4 above is used to determine $\rho_{as}(865)$, where *Kw* and *Ka* are:

$$Kw= [\rho_w(885)*t(885)]/[\rho_w(865)* t(865)] \quad \text{(H7)}$$

$$Ka=(885/865)^\alpha \quad \text{(H8)}$$

A new estimate of $\rho_w(865)$ is obtained from the $\rho_{as}(865)$ estimated by the difference equation as:

$$\rho_w(865)= (\rho_{rc}(865)- \rho_w(865))/t(865) \quad \text{(H9)}$$

An estimate of $\rho_w(865)$ <= zero is treated as an exception and the BPAC fails. The procedure then proceeds to the next iteration. On successful completion $\rho_w(705,775,885)$ are calculated according to (H2,H3,H3) and $bb_p(775)$ is preserved in order to estimate TSM.

4.4.10 Estimate combination

Where there is an estimate from both band sets the output is a simple arithmetic average. This may be upgraded in future to blend the data according to the final reflectance values. Note, both $bb_p(775)$ is also an average for subsequent estimates of TSM.

4.4.11 TSM Estimates

TSM is estimated as:

$$TSM = bb_p(775)/bb_p^*(775) \quad \text{(S7)}$$

4.4.12 ODESA output

The SPM derived from the BPAC is available as the netCDF product SPM_BR from ODESA (Optical Data processor of the ESA, http://earth.eo.esa.int/odesa/). A number of intermediate variables are also available and the description / definition of these can be found in the corresponding MERIS DPM.

4.4.13 Derived flags

In the third reprocessing the BPAC is turned on at all times, and the radiometric threshold is not used. Therefore, the BPAC flag indicates successful convergence of the BPAC.

The CASE2_S flag, which indicates high scattering is raised when the TSM calculated in (S7) is greater than 0.75mg.l^{-1}. It should be noted that this flag reflects scattering in the NIR and as such does not strictly refer to the Case 1 / Case 2 distinction, since the flag can be raised by high levels of phytoplankton in mesotrophic waters. The flag is dependent on the successful completion of the BPAC.

5. Parameter Description

Symbol	Descriptive Name	I/O	Range/Reference/Remarks
$t([705,775,865,885],\theta_v,\theta_s,\Delta_\phi)$	Atmospheric diffuse transmittance	I	From Rayleigh Correction
$F(\lambda,a,bb_w,bb_p,\theta_v,\theta_s,\Delta_\phi)$[1]	Water reflectance above surface factor - polynomials	I	Database Lookup Table
a(TSM)	Sediment absorption	I	Database Lookup Table
b(TSM)	Sediment backscatter	I	Database Lookup Table

c	Aerosol extrapolation parameter	-	Calculated Internally
$\rho_{as}([705,775,865],\theta_v,\theta_s,\Delta_\phi)$	Single scattering reflectance	I	From Rayleigh Correction
$\rho_{as}([705,775,865],\theta_v,\theta_s,\Delta_\phi)$	Single scattering corrected reflectance	O	From Iterative Procedure
$\varepsilon(705,865,\theta)$	ρ_{rc} Ratio	-	Calculated Internally
$\varepsilon(775,865,\theta)$	ρ_{rc} ratio	-	Calculated Internally
TSM	Sediment load	-	From Procedure
θ_s	Solar zenith angle	I	From Navigation
Δ_ϕ	Azimuth difference	I	From Navigation
θ_v	Viewing angle	I	From Navigation
$\theta \equiv [\theta_v,\theta_s,\Delta_\phi]$	Viewing / solar angles	-	Naming Convention

5.1.1 Error Budget Estimates

Within Lavender *et al.* (2005) a set of simulated ρ_{rc} data were generated to test the BPAC iterative inversion method. The simulated data had a uniformly distributed set of viewing geometries, TSM concentration varied randomly between 0.1 and 200 g m^{-3} and $\rho'_a(865)$ was allowed to vary uniformly between 0.005 and 0.030. Varying amounts of noise (between 0 and 5%) were introduced to the modelled ρ_{rc} values for NIR bands to simulate absolute SeaWiFS measurement uncertainties. The retrieval performance was excellent when there was no measurement noise: the mean difference was <0.2%, root-mean-square (RMS) difference was ~10% and over 95% of the retrievals were within 20% of the actual value. At 0.5% noise, the RMS difference increased to ~30% and less than 70% of the retrievals were within 20%. At 5% noise, the RMS error in the retrieval was more than 25% and <30% of the retrievals were within 20% of the actual values.

5.1.2 Practical Considerations

The algorithm requires LUTs and is performed on a pixel-by-pixel basis.

5.1.3 Sensitivity to IOPs

Results (e.g. Bale *et al.*, 1994) show that although the exact value of TSM iterated within the turbid water correction procedure may vary according to sediment properties, the relationships between the remote sensed reflectances are robust and independent of sediment type.

5.2 Practical Considerations

5.2.1 Calibration and Validation

The low band set method has also been validated using MODIS (Blondeau-Patissier *et al.*, 2004) and SeaWiFS (Blondeau-Patissier *et al.*, 2004 and Lavender *et al.*, 2005).

Figure 15 shows images from the Severn estuary processed using the BPAC from the original model (ATBD v4.1), and the new version (ATBD v5.0). The new version was implemented in MEGS; neither vicarious calibration or ICOL were used. At the upper part of the Severn (pin 5) concentrations of TSM can reach in excess of 100 $g.m^{-3}$. The original version shows areas of white at the top of the estuary where the BPAC failed, in contrast the new version that shows a clear gradient to the top of the estuary.

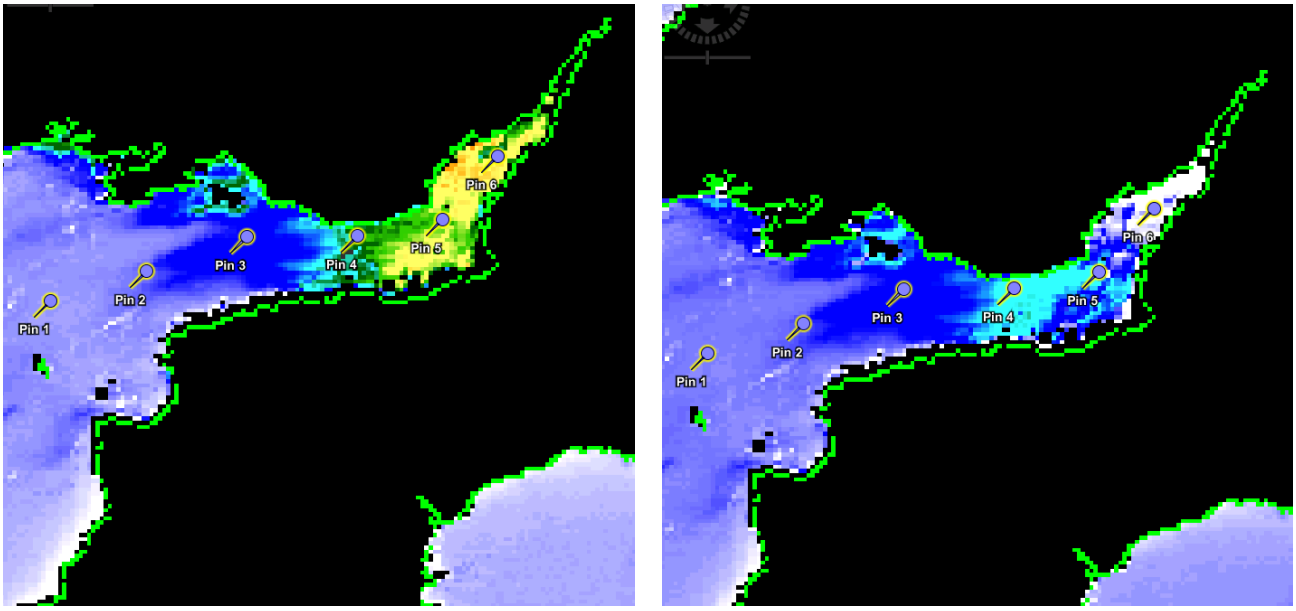

a) $\rho_w(705)$ scaled 0→0.12 (white zero) – this ATBD

b) $\rho_w(705)$ scaled 0→0.12 (white zero) – original mode as used in Lavender *et al.* (2005)

Figure 17: $\rho_w(705)$ images from v5.0 and v4.1

Data were extracted from a transect along the pins and are shown in Figure 16 and Figure 17. In the transect, decreasing longitude can be taken as a proxy for TSM. Figure 16 shows that the new version continued to retrieve a sensible estimate of $\rho_w(775)$ along the whole transect, whereas the old version never retrieved a $\rho_w(775)$ of greater than 0.01 – the expected limit of the BPAC low band set. The results are less encouraging for α, although the new version of the BPAC did return a value albeit high. It should also be noted the failure in the determination of α occurred at a lower longitudes in the new version. At lower TSM concentrations the retrievals were similar indicating that the new iterative routine achieved results consistent with the old routine.

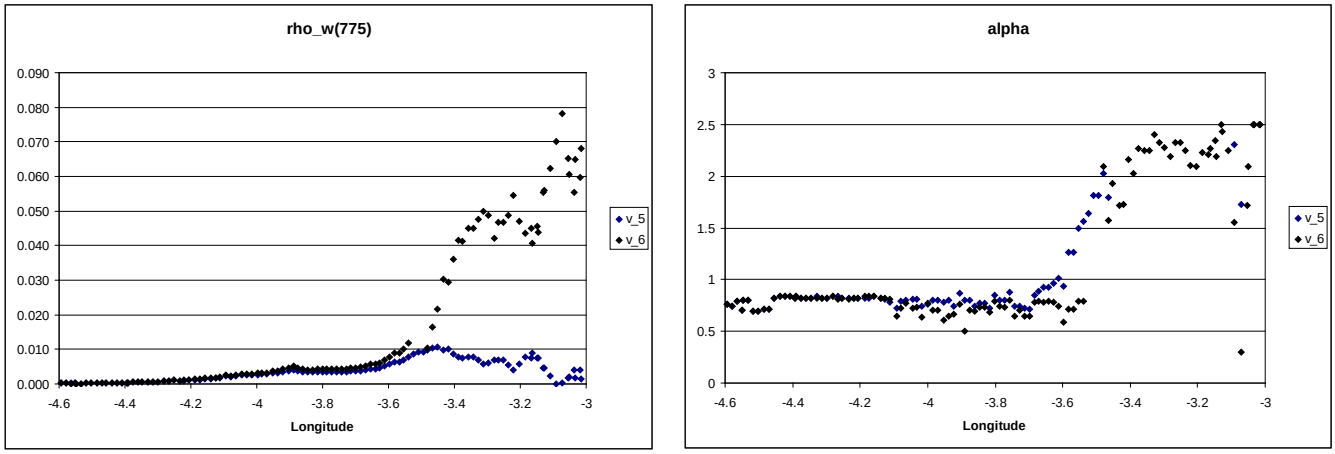

a $\rho_w(775)$ determined by v5.0 and v4.1 b α determined by v5.0 and v4.1

Figure 18: $\rho_w(775)$ and α retrievals for Severn transect

The results from the visible bands shown in Figure 17 show the expected failure; however the results (a) from the new version are encouraging, since at least $\rho_w(490)$ is always positive.

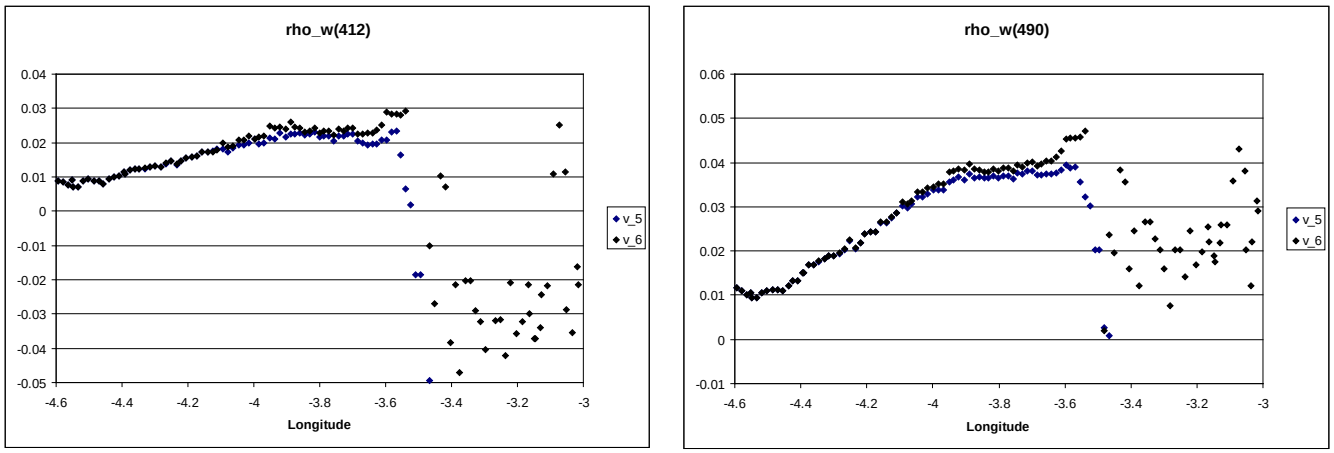

a $\rho_w(412)$ determined by v5.0 and v4.1 b $\rho_w(490)$ determined by v5.0 and v4.1

Figure 19: $\rho w(412)$ and $\rho w(490)$ retrievals for Severn transect

In conclusion, the figures show that the basic test of the new BPAC indicates that the algorithm is functional, and thus provides a preliminary validation. There are remaining issues in the high band set estimate, but these may be resolved by increased accuracy of the calibration at 885 am, a band that has not previously been used for bio-optical algorithms. In addition, there are still doubts about the appropriate sediment IOPs for this band.

5.2.2 Quality Control and Diagnostics.

Certain very high sediment waters or extreme atmosphere types could return anomalous results. Both of these could be classified as cloud / land because of their high absolute reflectance. Lavender *et al.* (2005) showed that for SeaWiFS a non-unique solution to the inversion problem became more problematic at TSM concentrations greater than circa 50 g m^{-3}, The use of the upper band set improves this, and the expected performance is around 500 g m^{-3} before ambiguity occurs.

5.2.3 Exception Handling

Potentially, the iterative solution can produce either infinite or negative reflectances. This event should be trapped as an AC failure. Lavender *et al.* (2005) showed that for SeaWiFS the number of negative pixels was reduced when applying the BPAC and failures accounted for less than 12% of the total pixels processed by the BPAC method; used a threshold of $\rho_w(670) > 0.003$ for detecting potentially bright pixels.

5.2.4 Output Product

Atmospheric reflectance in NIR and TSM for Case 2 flagging.

6. Assumptions and Limitations

The algorithm needs to be tested on a range of simulated data atmospheric data to consider a number of aerosol types. At present, knowledge of NIR absorption is limited and needs to be improved using Mie modelling.

7. References

Antoine, D. and A. Morel, 1999. A multiple scattering algorithm for atmospheric correction of remotely-sensed ocean colour (MERIS instrument): principle and implementation for atmospheres carrying various aerosols including absorbing ones. *International Journal of Remote Sensing,* 20(9): 1875-1916.

Arnone, R.A., Martinolich, P., Gould, R.W., Stumpf, R. and S. Ladner, 1998. Coastal optical properties using SeaWiFS. In *SPIEE Ocean Optics XIV,* edited by S. Ackleson and Cambell.

Bale, A.J., Tocher, M.D., Weaver, R., Hudson, S.J. and J. Aiken, 1994. Laboratory measurements of the spectral properties of estuarine suspended particles. *Netherlands Journal of Aquatic Ecology*, 28**:** 237-244.

Blondeau-Patissier, D., Tilstone, G.H., Martinez-Vicente, V. and G.F. Moore, 2004. Comparison of bio-physical marine products from SeaWiFS, MODIS and a bio-optical model with in situ measurements from Northern European waters. *Journal of Optics A: Pure and Applied Optics*, 6: 875–889.

Bricaud, A., A. Morel, M. Babin, K. Allali And H. Claustre, 1998. Variations of light absorption by suspended particles with Chlorophyll-a concentration in oceanic (case 1) waters: Analysis and implications for bio-optical models, *Journal of Geophysical Research*, 103: 31033-31044

Gordon, H.R, 1979). Diffuse reflectance of the ocean: the theory of its augmentation by chlorophyll a fluorescence at 685 nm. *Applied Optics*, 18: 1161-1166.

Gordon, H.R., and M. Wang, 1994. Retrieval of water-leaving radiances and aerosol optical thickness over the oceans with SeaWiFS: a preliminary algorithm. *Applied Optics*, 33: 443-452.

Kou, L., D. Labrie, et al. 1993. Refractive indices of water and ice in the 0.65-2.5 μm spectral range. *Applied Optics* 32: 3531-3540.

Lavender, S.J., 1996. Remote Sensing of Suspended Sediment. PhD Thesis. Institute of Marine Studies, University of Plymouth and in collaboration with Plymouth Marine Laboratory.

Lavender, S.J., Pinkerton, M.H., Moore, G.F., Aiken, J and D. Blondeau-Patissier, 2005. Modification to the Atmospheric Correction of SeaWiFS Ocean Colour Images over Turbid Waters. *Continental Shelf Research* 25: 539-555.

Mobley, C.D., 1995. *Hydrolight 3.0 Users Guide*, SRIRI Project 5632. SRI International, Menlo Park, CA, United States.

Moore, G.F., Aiken, J., and S.J. Lavender, 1999. The atmospheric correction of water colour and the quantitative retrieval of suspended particulate matter in Case II waters: application to MERIS. *International Journal of Remote Sensing* 20(9): 1713-1733.

Morel, A. and B. Gentili, 1993. Diffuse reflectance of oceanic waters, II. Bidirectional aspects. *Applied Optics* 32(33): 6864–6879.

Morel, A., 1974. Optical properties of pure seawater. *Optical aspects of Oceanography*. Ed Jerlov, N.G. and Nielsen, S.E. Academic Press: London.

Petzold, T.J., 1972. Volume scattering functions for selected ocean waters. *Scripps Inst. Oceanogr. Rep.* 72-78**:** 79.

Pope, R.M. and E.S Fry, 1997. Absorption spectrum (380–700 nm) of pure water, IIII. Integrating cavity measurements. *Applied Optics*, 36: 8710–8723.

Press, W.H., Teukolsky, S.A., Vetterling, W.T. and B.P. Flannery, 1992. *Numerical Recipes in C*, Second Edition, Cambridge University Press, 994.

Ruddick, K. G., V. De Cauwer, et al. 2006. Seaborne measurements of near infrared water-leaving reflectance: The similarity spectrum for turbid waters. *Limnology and Oceanography 51*: 1167-1179.

Ruddick, K.G., Ovidio, F. and M. Rijkeboer, 2000. Atmospheric correction of SeaWiFS imagery for turbid and inland waters. *Applied Optics* 39: 897-912.

Siegel, D.A., Wang, M., Maritorena, S. and W. Robinson, 2000. Atmospheric correction of satellite ocean color imagery: the black pixel assumption. *Applied Optics* 39: 3582-3591.

Stumpf, R.P., Arnone, R.A, Gould, R.W., Martinolich, P. and V. Ransibrahmanakul, 2002. A partially-coupled ocean-atmosphere model for retrieval of water-leaving radiance from SeaWiFS in coastal waters. In *Algorithm Updates for the Fourth SeaWiFS Data Reprocessing*, Vol. 22, S. B. Hooker and E. R. Firestone, eds. (NASA Tech. Memo. 2002-206892, NASA Goddard Space Flight Center, Greenbelt, MD, 2003).

Wang, M. and W. Shi, 2005. Estimation of ocean contribution at the MODIS near-infrared wavelengths along the east coast of the U.S.: Two case studies. *Geophysical Research Letters* 32: L13606.

Whitlock, C.H., Poole, L.R., Usry, J.W., Houghton, W.M., Witte, W.G., Morris, W.D. and E.A. Gurganus, 1981. Comparison of reflectance with backscatter and absorption parameters for turbid waters. *Applied Optics*, 20: 517-522.

SUMMARY SHEET

Product Name	Case II.S (Sediment) Bright Water Correction.
Product Code	Internal to ocean atmospheric correction.
Product Level	2
Product Parameters	
Spatial Coverage	Coastal waters, coccolithophore blooms and mesotrophic waters.
Packaging	
Units	Reflectance – dimensionless, TSM $g.m^{-3}$
Range	
Sampling	
Resolution	Any
Accuracy	Estimates from tests with CASI data indicated that the accuracy is within the radiometric calibration of CASI (±5%). For simulated data and 5% noise, the RMS error in the retrieval was more than 25% and <30% of the retrievals were within 20% of the actual values (see Section 4.1.1).
Geo-location Requirements	Angle of View
Format	Internal I/O
Appended Data	
Frequency of Generation	As per atmospheric correction.
Size of Product	N/A [16bit if TSM output implemented]
Additional Information	

Identification of Bands	[705,775,865,895]
Assumptions on MERIS Input Data	Rayleigh Corrected and gaseous absorption corrected.
Output Data	ρ_{as}*[705,775,865,895], TSM estimate for flagging.*
Identification of Ancillary and Auxiliary Data	Temperature climatology and MERIS actual wavelength for smile and temperature aw correction.
Assumptions of Ancillary and Auxiliary Data	Temperature +/- 2°C